

3D ATAC-PALM: super-resolution imaging of the accessible genome

Liangqi Xie^{1,2,3,8}, Peng Dong^{1,8}, Xingqi Chen^{4,7}, Tsung-Han S. Hsieh^{2,3}, Sambashiva Banala¹, Margherita De Marzio⁵, Brian P. English¹, Yifeng Qi⁵, Seol Kyoung Jung⁶, Kyong-Rim Kieffer-Kwon⁶, Wesley R. Legant¹, Anders S. Hansen¹, Anton Schulmann¹, Rafael Casellas⁶, Bin Zhang¹, Eric Betzig¹, Luke D. Lavis¹, Howard Y. Chang¹, Robert Tjian^{1,2,3} and Zhe Liu¹

To image the accessible genome at nanometer scale *in situ*, we developed three-dimensional assay for transposase-accessible chromatin-photoactivated localization microscopy (3D ATAC-PALM) that integrates an assay for transposase-accessible chromatin with visualization, PALM super-resolution imaging and lattice light-sheet microscopy. Multiplexed with oligopaint DNA-fluorescence insitu hybridization (FISH), RNA-FISH and protein fluorescence, 3D ATAC-PALM connected microscopy and genomic data, revealing spatially segregated accessible chromatin domains (ACDs) that enclose active chromatin and transcribed genes. Using these methods to analyze genetically perturbed cells, we demonstrated that genome architectural protein CTCF prevents excessive clustering of accessible chromatin and decompacts ACDs. These results highlight 3D ATAC-PALM as a useful tool to probe the structure and organizing mechanism of the genome.

Genome conformation and nuclear organization play profound roles in gene expression, DNA replication and DNA repair¹. Chromosome conformation capture (3C) based deep sequencing methods have provided important insights into genome organization modules (compartments, topologically associated domains (TADs) and loop domains) with rich sequence information^{2–5}. However, the extensive heterogeneity and intrinsic variation of genome folding⁶ prompts the development of new imaging methods to investigate the 3D genome organization in single cells.

Of the ~6 billion base pairs of DNA in the diploid human genome, only a small fraction (~2%) is accessible to the binding of transcription factors, cofactors, RNA polymerases and others, which decode essential genetic information to instruct precise spatiotemporal gene expression programs⁷. The linear distribution of accessible chromatin (for example, enhancers, promoters and insulators) has been extensively mapped by DNase I digestion^{8,9} or by assay for transposase-accessible chromatin with high-throughput sequencing (ATAC-seq)^{10,11}. Recently, an assay for a transposase-accessible chromatin (ATAC)-based imaging method (ATAC-see) has been developed to visualize cell-type specific accessible chromatin in single cells by transforming the molecular accessibility of chromatin into fluorescent signal¹². However, because of the diffraction-limited resolution, this technique was unable to precisely pinpoint the accessible *cis*-regulatory chromatin and quantitatively characterize its 3D organizational pattern inside the compact nucleus. Here, we report the development of a 3D super-resolution imaging method, 3D ATAC-PALM, to capture the nanometer-scale 3D architecture of *cis*-regulatory elements in single cells and demonstrate its applications in investigating genome organization mechanisms.

Results

Super-resolution imaging of the accessible genome by 3D ATAC-PALM. To visualize the entire accessible genome on the nanometer scale, we reconstituted a recombinant, hyperactive Tn5 transposase coupled to bright photoactivatable Janelia Fluor 549 (PA-JF₅₄₉)¹³ conjugated DNA probes (Fig. 1a and Extended Data Fig. 1a,b). To preserve nuclear architecture and genome folding, we performed Tn5 PA-JF₅₄₉ labeling in formaldehyde-fixed mouse embryonic stem cells (ESCs). Consistent with the previous report¹², genome-wide deep sequencing (ATAC-seq) revealed that the efficiency and specificity of Tn5 PA-JF₅₄₉ labeling in fixed ESCs were comparable with those of Nextera Tn5 labeling in live cells. Specifically, DNA fragment lengths, transcription start site enrichments and ATAC-seq peak distributions of both Tn5 systems were highly comparable (Extended Data Fig. 1c–g), confirming that the Tn5 PA-JF₅₄₉ system efficiently and specifically catalyzed covalent insertion of PA-JF₅₄₉ DNA probes into the accessible genome (Fig. 1a). The PA-JF₅₄₉ DNA probes were to be used for super-resolution imaging of accessible chromatin by the PALM¹⁴.

To efficiently use the photon budget, we performed 3D PALM imaging using the lattice light-sheet microscope¹⁵ with submicrometer illumination thickness to suppress out-of-focus photobleaching and achieve improved signal-to-noise ratio for single-molecule detections throughout the nucleus (Fig. 1b). We also introduced astigmatism with the cylindrical lens in the detection path^{16,17} to generate an axially sensitive point-spread function (PSF) for improved axial localization (*z* localization precision was improved to around 50 nm) (Fig. 1b). Individual samples were imaged iteratively for at least 10,000 cycles (~24 h) to exhaust single-molecule detections. After drift correction, merging consecutive localization

¹Janelia Research Campus, Howard Hughes Medical Institute, Ashburn, VA, USA. ²Department of Molecular and Cell Biology, Li Ka Shing Center for Biomedical and Health Sciences, CIRM Center of Excellence, University of California, Berkeley, CA, USA. ³Howard Hughes Medical Institute, Berkeley, CA, USA. ⁴Center for Personal Dynamic Regulomes and Howard Hughes Medical Institute, Stanford University, Stanford, CA, USA. ⁵Departments of Chemistry, Massachusetts Institute of Technology, Cambridge, MA, USA. ⁶Lymphocyte Nuclear Biology, NIAMS and Center of Cancer Research, NCI, NIH, Bethesda, MD, USA. ⁷Present address: Department of Immunology, Genomics and Pathology, Uppsala University, Uppsala, Sweden. ⁸These authors contributed equally: Liangqi Xie, Peng Dong. [✉]e-mail: jmlim@berkeley.edu; liuz11@janelia.hhmi.org

events, nucleus segmentation based on a H2B-green fluorescent protein (-GFP) marker and carefully masking out mitochondrial DNA signals, we obtained roughly 50,000–100,000 effective 3D localizations per nucleus (Extended Data Fig. 2a,b). The number of effective localizations detected per nucleus is on the same order of the number of accessible regions identified in bulk and in single-cell ATAC-seq experiments¹¹. More importantly, reducing Tn5 PA-JF₅₄₉ labeling concentrations twofold did not significantly affect the number of effective localizations obtained in individual nuclei (Extended Data Fig. 2a), suggesting that the labeling of accessible genomic sites was saturated. We named this super-resolution accessible genome imaging strategy ‘3D ATAC-PALM’. It is important to note that only roughly 2% of the genome is accessible^{10–12}. Thus, the Tn5 PA-JF₅₄₉ labeling under nondenaturing conditions (37°C, neutral pH) in a chemically crosslinked nucleus is unlikely to perturb the overall chromatin structure.

3D ATAC-PALM reveals spatially segregated ACDs. After nucleus segmentation and localization-based image reconstruction, we found that accessible genomic regions in mouse ESCs and embryonic fibroblasts (MEFs) are nonhomogeneously distributed and organized into spatially segregated 3D clusters. Henceforth, we called these high-density clusters accessible chromatin domains (ACDs) (Fig. 1c and Supplementary Video 1). To quantify the degree of accessible chromatin clustering, we used the pair autocorrelation function $g(r)$ (equation (8)), which was applied by physicists to describe the clustering of stars in galaxies¹⁸. $g(r)$ measures the density of localizations on a 3D surface, at a distance of r from the reference point and is equal to 1 for uniformly distributed localizations (Fig. 1d). In our $g(r)$ calculation, we also used a previously described statistical model¹⁹ to suppress over-counting of single fluorophores due to photoblinking. We found that the $g(r)$ for ATAC localizations in both ESCs or differentiated MEFs was significantly higher than that of a uniform distribution at multiple length scales, indicating extensive spatial clustering of accessible chromatin (Fig. 1d and Extended Data Fig. 2c). In addition, ATAC localizations were significantly more clustered than histone H2B PALM localizations collected in the same imaging conditions (Fig. 1d), excluding the possibility that over-counting of blinking molecules could account for 3D clustering of accessible chromatin. We estimated the localization density enrichment at the center of ACDs $g(0)$ by fitting $g(r)$ with a fluctuation model (equation (16)) to obtain the clustering amplitude (A) (Fig. 1d). The typical radius of ACDs in wild-type (WT) ESCs was estimated by using Ripley’s H function, $H(r)$ (equation (13)). We found that $H(r)$ for ATAC localizations

significantly deviated from a uniform distribution ($H(r)=0$), reaching a maximum at a radius of roughly 150 nm (Fig. 1e). Consistent with these results, DBSCAN (density-based spatial clustering of applications with noise)²⁰ analysis identified much larger number (around 11-fold more) of ACDs from ATAC localizations than from uniformly sampled localizations in the same volume (Fig. 1f). It is worth noting that we did not detect significant differences of the $g(r)$ function at distinct interphase stages (for example, G1, S and G2) demarcated by genetically encoded cell cycle fluorescent reporters (Extended Data Fig. 2d,e)²¹.

To test whether the organization of accessible chromatin can be perturbed, we induced chromatin hyperacetylation by the HDAC inhibitor trichostatin A (TSA)²². TSA treatment markedly reduced $g(r)$ (Fig. 1d), suggesting less clustering and a more homogenous distribution of accessible chromatin in the nucleus. Genome-wide ATAC-seq revealed that TSA treatment not only induced the formation of a large number of new accessible sites in the genome but also reduced chromatin accessibility at enhancer and promoter regions, thus effectively diminishing the contrast of *cis*-regulatory element landscape in general (Extended Data Fig. 2f,g). These results indicated that 3D ATAC-PALM is sufficiently sensitive to detect organizational changes of accessible chromatin.

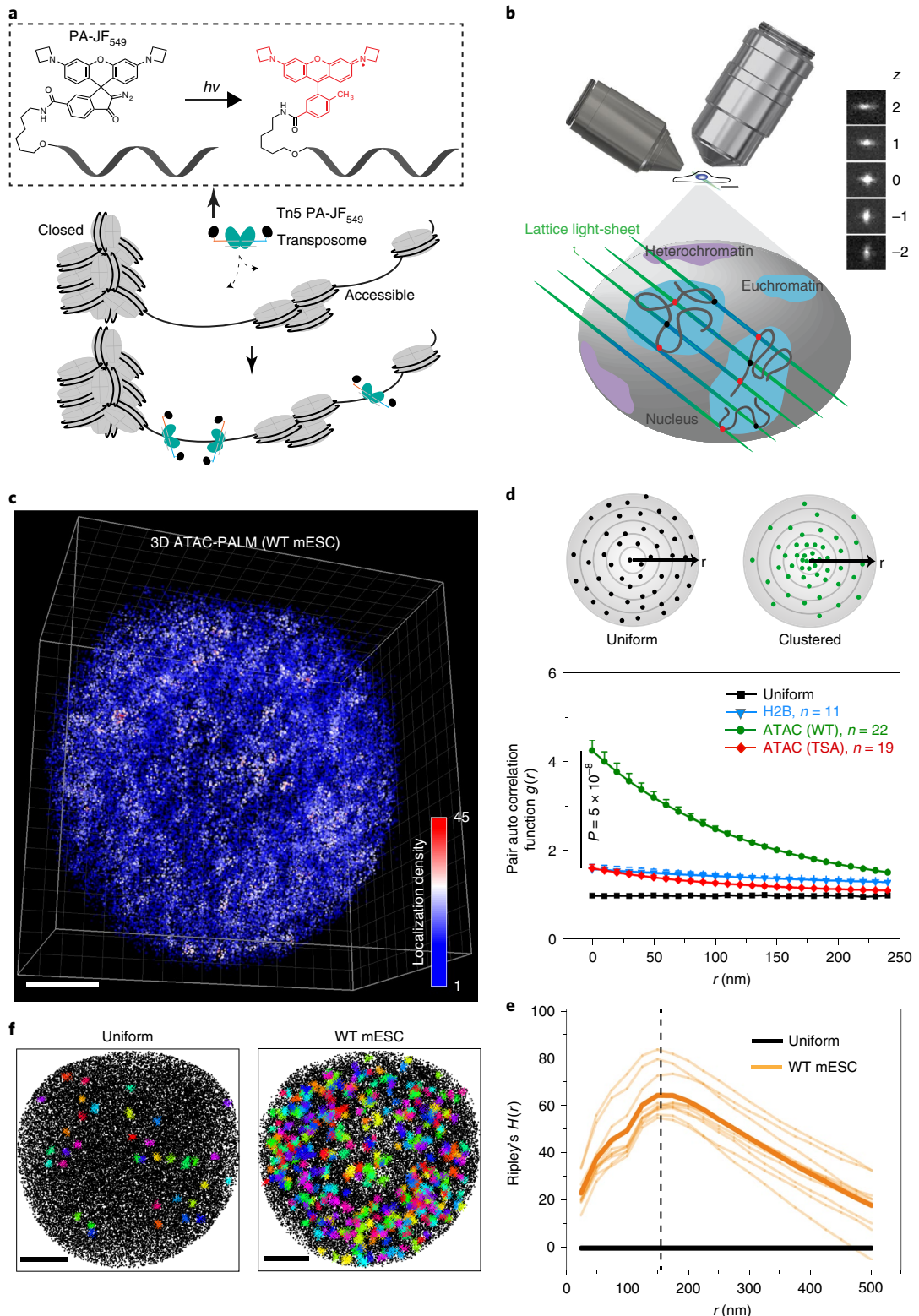
3D ATAC-PALM multiplexed with Oligopaint DNA-fluorescence in situ hybridization (FISH), RNA-FISH and protein fluorescence. To understand the nature of ACDs, we sought to simultaneously image ACDs and other key features defined from genomic data (for example, ATAC-seq, ChIP-seq and Hi-C). To this end, we optimized the compatibility of 3D ATAC-PALM with available single-cell imaging techniques such as Oligopaint DNA-FISH, RNA-FISH and protein fluorescence (see detailed protocols in Supplementary Methods) (Fig. 2a). For example, by coupling 3D ATAC-PALM with Oligopaint DNA-FISH that uses high-density fluorescent oligo probes to label a particular genomic region^{23–27}, we found that individual ACDs were statistically prone to spatially colocalize with active (ATAC and H3K4me3-rich) genomic regions (Fig. 2b,c and Supplementary Videos 2 and 3) and were spatially segregated from inactive (ATAC and H3K4me3-poor) regions (Fig. 2d). We noted that high temperature, denaturing conditions used in DNA-FISH^{23–27} did not significantly alter the $g(r)$ function relative to that for the nondenaturing ATAC labeling condition, suggesting that the clustering pattern of ATAC localizations was preserved after DNA-FISH (Extended Data Fig. 3d). Moreover, because of the saturated labeling and localization detection in our imaging (Extended Data Fig. 2a), the density variation of ATAC

Fig. 1 | Visualizing the accessible genome topology by 3D ATAC-PALM. **a**, Schematics of the 3D ATAC-PALM labeling and imaging strategy. PA-JF₅₄₉ was conjugated to DNA oligo containing the mosaic ends of the Tn5 transposon and reconstituted with Tn5 transposase (cyan) to form the active transposome complex in vitro. The cells were fixed, permeabilized and accessible sites in the genome were selectively labeled by the Tn5 PA-JF₅₄₉ transposome. Photoactivation (hv represents photon energy, 405 nm laser) of the nonfluorescent PA-JF₅₄₉ yields highly fluorescent methyl-substituted JF₅₄₉. **b**, Tn5 PA-JF₅₄₉ transposome-treated cells were mounted onto the lattice light-sheet microscope for 3D ATAC-PALM imaging. A cylindrical lens was introduced to precisely estimate the z coordinates based on the ellipticity of the fluorescent signal. Each z step represents 271 nm distance. **c**, 3D illustration of accessible chromatin localizations in WT mouse ESCs. The color-coded localization density was calculated with a canopy radius of 250 nm. A total of $n=22$ cells from four biologically independent experiments were imaged with similar results. Scale bar, 2 μm. **d**, Global pair autocorrelation function $g(r)$ analysis of ATAC localizations for WT and TSA treated mESCs. The top panel shows a simplified two-dimensional scheme for uniform (black dots, top left) or clustered (green dots, top right) distribution of localizations. $g(r)$ represents the pair autocorrelation function of distance r calculated from a given origin point inside the space. The $g(r)$ for 3D H2B-HaloTag PALM localizations was computed as a control. The error bars represent standard error of the mean (s.e.m.). The two-sided nonparametric Mann-Whitney U -test was used to compare the clustering amplitude A (equals $g(0)$) in different groups. $g(r)$ was plotted from the fitted exponential decay function. **e**, Ripley’s H function $H(r)$ of the ACDs from WT mESCs. The black line indicates uniform distribution and the light-yellow lines represent the $H(r)$ from individual WT mESCs ($n=10$) and the thick yellow line indicate their mean. The vertical dashed line represents the peak radius position around 150 nm. **f**, Identification of ACDs by DBSCAN algorithm. Both panels show the z-projection of all the localizations (black dots) and identified clusters (colored crosses). Left panel, as computational control, DBSCAN only detected 36 clusters in uniformly sampled data points with the same average density as in the right panel. Right panel, DBSCAN identified 402 clusters in WT ESCs in one 3D ATAC-PALM experiment. A total $n=22$ cells from three biological replicates were used in the analysis. Scale bars, 2 μm. Statistics source data are provided in Source Data Fig. 1.

localizations in individual chromatin segments likely reflects the extensive heterogeneity and intrinsic variation of genome folding observed in single cells⁶ (Fig. 2f). To further investigate whether ACDs are spatially correlated with active chromatin, we coupled 3D ATAC-PALM with RNA-FISH and found that ACDs enclosed an actively transcribed pluripotency marker gene, *Nanog* (Fig. 2e,f).

To overcome the specificity and resolution limitations of antibody-based imaging, we generated genome-edited mESC lines in which we fused the HaloTag to endogenous regulatory proteins

associated with active chromatin (for example, histone variant H2A.Z and Mediator subunit 1 (MED1))^{28,29} (Extended Data Fig. 3a,b). After accessible chromatin and HaloTag labeling with PA-JF₅₄₉ and PA-JF₆₄₆ (ref. ¹³), respectively, we performed two-color, super-resolution 3D PALM imaging. Pair cross-correlation analysis revealed that localizations of H2A.Z or MED1 were spatially correlated with ATAC localizations across multiple scales (Extended Data Fig. 3c,e–i). In contrast, ACDs and HP1-GFP labeled heterochromatic regions were mutually exclusive, organized into distinct



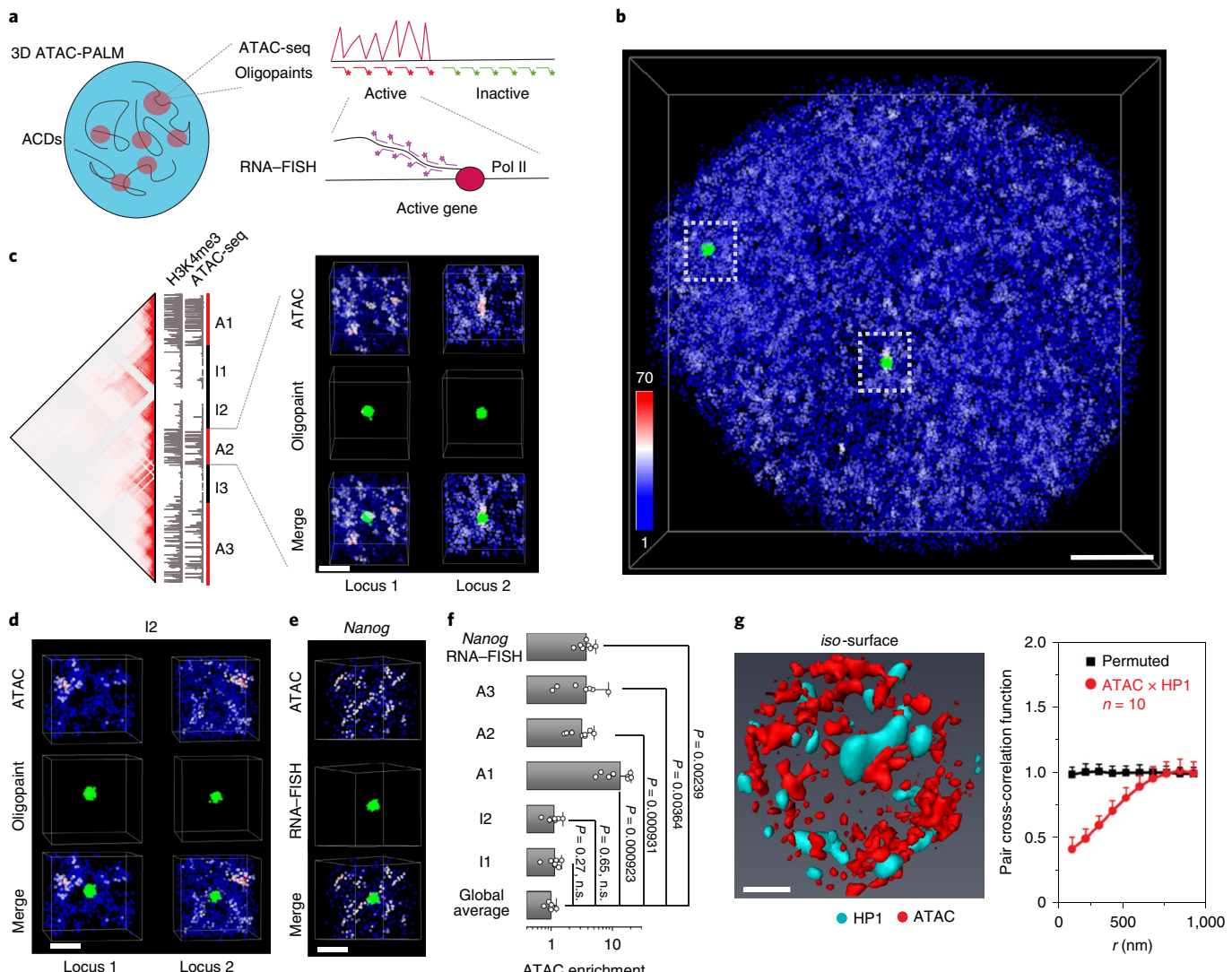


Fig. 2 | ACDs are associated with active chromosomal segments. **a**, Schematics showing multiplexed imaging of 3D ATAC-PALM and Oligopaint DNA-FISH or RNA-FISH. **b**, Colocalization of ACDs with ATAC-rich segments. Single-cell illustration of two-color imaging of 3D ATAC-PALM (red) and 3D Oligopaint DNA-FISH (green) targeting an ATAC-rich segment (A2) as shown in the left of **c**. Scale bar, 2 μm. **c**, (Left panel) Alignment of Hi-C heatmap, ATAC-seq and H3K4me3 tracks surrounding the pluripotency gene *Nanog* on Chromosome 6 (chr6:120080000-125240000). ATAC-rich segments with higher density of ATAC and H3K4me3 peaks are underlined by red bars (A1, A2 and A3). Conversely, low ATAC density and H3K4me3-poor segments are underlined by black bars (I1, I2 and I3). See details of these domain coordinates in the supplementary information. (Right panel) Top, zoom-in view of the ATAC localizations detected by 3D ATAC-PALM imaging in the active region A2. Middle, the zoom-in view of the Oligopaint DNA-FISH signals of two alleles. Bottom, zoom-in view showing the colocalization between ACDs and ATAC-rich segments (green) labeled by 3D Oligopaint DNA-FISH probes for both alleles in the cell. Scale bar, 1 μm. **d**, ACDs are spatially separated from ATAC-poor segments. Top, zoom-in view of the ACDs detected by 3D ATAC-PALM imaging. Middle, the zoom-in view of the Oligopaint DNA-FISH signals of two alleles (I2). Bottom, zoom-in view shows spatial separation of ACDs from ATAC-poor segments (green) labeled by 3D Oligopaint DNA-FISH probes for both alleles in the cell. Scale bar, 1 μm. **e**, ACDs enclose actively transcribed gene *Nanog*. Top, zoom-in view of the ACDs detected by 3D ATAC-PALM imaging. Middle, the zoom-in view of the RNA-FISH signals of the *Nanog* gene (A2 region) using intronic probes marking the transcription site. Bottom, zoom-in view shows that the actively transcribed *Nanog* gene is enclosed inside the high-density accessible chromatin region. Representative images in **b–e** are from two biologically independent experiments with similar results. Scale bar, 1 μm. **f**, ATAC localizations were significantly enriched in ATAC-rich segments (A1, A2 and A3) labeled by 3D Oligopaint DNA-FISH probes and in actively transcribed regions (*Nanog* RNA-FISH) but not in ATAC-poor segments (I1 and I2). Specifically, the plot represents the log scale fold enrichment for ATAC localizations in the DNA-FISH or RNA-FISH labeled regions over the average density in the nucleus. The error bar represents s.d. Each dot represents one analyzed locus for each condition. Statistical tests were performed by using a two-sided nonparametric Mann-Whitney U-test. **g**, ACDs are spatially segregated from heterochromatin regions. Left, 3D spatial relationship between accessible chromatin (red, Gaussian blurred) and heterochromatin (turquoise, HP1α-GFP). Scale bar, 2 μm. Right, two-dimensional pair cross-correlation (x) function calculated for accessible chromatin (red) and heterochromatin (turquoise) regions. The curve represents the mean of pair cross-correlation function values across two-dimensional slices from $n=10$ cells and the error bars represent s.e.m. Statistics source data are provided in Source Data Fig. 2.

salt-and-pepper spatial patterns in the nucleus (Fig. 2g and Supplementary Video 4). Taken together, these results validated that ACDs revealed by 3D ATAC-PALM represent structures of active,

accessible chromatin that are spatially segregated from heterochromatin. Meanwhile, we also demonstrated that 3D ATAC-PALM can be coupled with other single-cell imaging techniques (such as

Oligopaint DNA–FISH, RNA–FISH, protein fluorescence-based super-resolution imaging) to study genome organization.

CTCF prevents excessive clustering of accessible chromatin.

To further understand the mechanism underlying the spatial organization of ACDs, we focused on genome architectural protein CTCF³⁰. To deplete CTCF with minimal secondary effects, we used the auxin-inducible degron (AID) system³¹ and tagged endogenous CTCF with a HaloTag-mini-AID (mAID) in a mESC line stably expressing the rice F-box protein TIR1 (Fig. 3a). The HaloTag-mAID was fused to the N terminus of CTCF to avoid previously reported problems (for example, auxin independent degradation and interference with CTCF function) associated with C-terminal tagging³². We found that HaloTag-mAID labeling of CTCF influenced neither basal protein levels (Extended Data Fig. 4a) nor cell proliferation before auxin treatment (Extended Data Fig. 4e–g). Within a few hours of auxin treatment, CTCF expression was undetectable by western blot, single-cell fluorescence imaging or flow cytometry (>99% depletion) (Fig. 3a and Extended Data Fig. 4a–d). The depletion was reversible, as CTCF protein levels quickly recovered after auxin washout (Extended Data Fig. 4d). Acute loss of CTCF (up to 12 h) did not cause noticeable changes in proliferation, cell cycle phasing or expression of pluripotency markers (Fig. 3a and Extended Data Fig. 4a,c,e–g), although prolonged CTCF (>48 h) loss did compromise proliferation, colony formation and survival of ESCs (Extended Data Fig. 4e–g).

Acute loss of CTCF triggered prominent organizational changes in ACDs (Fig. 3b and Supplementary Video 5) and markedly enhanced accessible chromatin clustering as the $g(r)$ function increased significantly across multiple length scales relative to unperturbed conditions (Fig. 3c). We found that, at the single-cell level, the efficiency of CTCF depletion was positively correlated with the degree of accessible chromatin clustering ($1/A$, equals $1/g(0)$) (Fig. 3d). Furthermore, the increase in accessible chromatin clustering induced by CTCF depletion was largely reversed when CTCF levels recovered after auxin washout (Extended Data Fig. 5a). As a control, genome-wide ATAC-seq revealed that acute loss of CTCF did not significantly affect chromatin accessibility at enhancers and promoters, although chromatin accessibility at CTCF binding sites was reduced (Extended Data Fig. 5b–f). Consistent with these results, DBSCAN analysis revealed higher ATAC localization densities in individual ACDs (Extended Data Fig. 5g), indicating that CTCF might regulate compaction of accessible chromatin.

Fig. 3 | Structural variation of accessible chromatin upon acute loss of CTCF. **a**, Acute depletion of CTCF in mESCs by the auxin-induced degradation system. Upper panel, the fusion of mini-AID (mAID)-HaloTag (Halo) to the N terminus of *Ctcf* in a mouse ESC line stably expressing osTir1. Lower panel, rapid degradation of CTCF on the addition of auxin revealed by immunofluorescence (lower panel). OCT4 immunostaining was used as a control. $n=2$ biological replicates. Scale bar, 5 μ m. **b**, Single-cell 3D illustration of ATAC localizations on CTCF depletion (CTCF($-$)). The inset shows ATAC localizations of a cell without CTCF depletion (CTCF(+)) for comparison. The color bar indicates localization density calculated by using a canopy radius of 250 nm. For the CTCF(+) condition, The inset panel used the localization density bar scaling from 1 to 50. The average localization density is the same for both cells. Experiments were repeated three times with similar results. Scale bar, 2 μ m. **c**, CTCF depletion promotes global accessible chromatin clustering. The error bar represents s.e.m. and two-sided Mann–Whitney *U*-test was applied for comparing data points at $g(0)$. **d**, The dose-dependent effect of CTCF depletion on global accessible chromatin clustering revealed by the inverse relationship between clustering amplitude (A) and residual CTCF levels measured by GFP-mAID-CTCF fluorescence intensities (arbitrary fluorescent units). A linear regression model was applied to derive the correlation of determination, R^2 . **e**, Representative iso-surfaces of an ATAC-rich segment (R5, red) before ($-$) and after (+) CTCF depletion (12 h). Scale bar, 1 μ m. Representative images are from $n=3$ biological replicates with similar results. **f**, Violin plot of 3D volumes (the number of voxels) of six ATAC-rich segments (R1–R6) before and after CTCF depletion. Throughout the volume measurements in this study, each voxel size is $x=48.9$ nm, $y=48.9$ nm and $z=199$ nm. The number of alleles analyzed is indicated at the bottom. The black bar indicates the median value for each data set and two-sided Mann–Whitney *U*-test was applied for statistical test. P values for R1–R6 are: $P=0.00839$ for R1, $P=1.17 \times 10^{-6}$ for R2, $P=6.26 \times 10^{-6}$ for R3, $P=4.97 \times 10^{-7}$ for R4, $P=0.00166$ for R5 and $P=2.51 \times 10^{-6}$ for R6. **g**, Top panel, schematic of the high-resolution Micro-C experiment. Lower panel, snapshots of Micro-C contact maps in auxin-mediated CTCF depletion (6 h) cells on chr1:132.5M–134.5 M at 8-kb resolution. **h**, Differential contact probability in compartments A and B. Differential contact probability was calculated by dividing the genome-wide decaying curve of CTCF depletion condition (+auxin) over nondepleted control ($-$ auxin). Statistics source data are provided in Source Data Fig. 3.

CTCF decompacts ACDs. To investigate the link between CTCF and chromatin compaction, we labeled six active and five inactive chromosomal segments that were well-demarcated based on chromatin accessibility and CTCF binding with high-density Oligopaint FISH probes (Extended Data Fig. 6a,b). We measured the 3D volume for each segment after *iso*-surface based segmentation of Airyscan images (Supplementary Video 6). We found that, after length normalization, active segments generally occupied larger volumes relative to inactive segments (Extended Data Fig. 6c), in good agreement with previously published STORM imaging results²⁵. Consistent with the increased clustering and higher localization density of accessible chromatin within ACDs, 3D volumes of active segments were significantly reduced, whereas inactive segments appeared largely unaffected upon CTCF depletion (Fig. 3e,f, and Extended Data Fig. 6d,e).

To further validate our single-cell imaging data, we performed high-resolution Micro-C experiments after acute CTCF depletion (6 h) in ESCs^{33,34} (Fig. 3g). Consistent with previous Hi-C results³⁰, we found that the number of chromatin loops and that of TADs were significantly reduced after CTCF loss whereas A/B compartments remained largely intact (Fig. 3g and Extended Data Figs. 7 and 8). Notably, CTCF depletion significantly enhanced contact probabilities within active chromatin segments but not within inactive ones (Fig. 3h), in good agreement with our 3D ATAC-PALM and Oligopaint DNA–FISH imaging data that CTCF depletion enhanced accessible chromatin clustering and compacted ACDs. These results are also consistent with predictions from the proposed loop extrusion model^{35–37}. Specifically, without adequate insulation by CTCF, cohesin continues to extrude chromatin DNA, resulting in compaction of accessible chromatin. However, due to the lack of CTCF binding at inactive (ATAC-poor) regions, CTCF depletion would not induce chromatin compaction at these regions just as what we observed here (Fig. 3h and Extended Data Fig. 6d,e). Thus, in addition to providing supportive evidence to previous modeling predictions based on Hi-C genomic data^{30,36,38}, these single-cell imaging results further underscored the potential of 3D ATAC-PALM as a tool to probe genome organization.

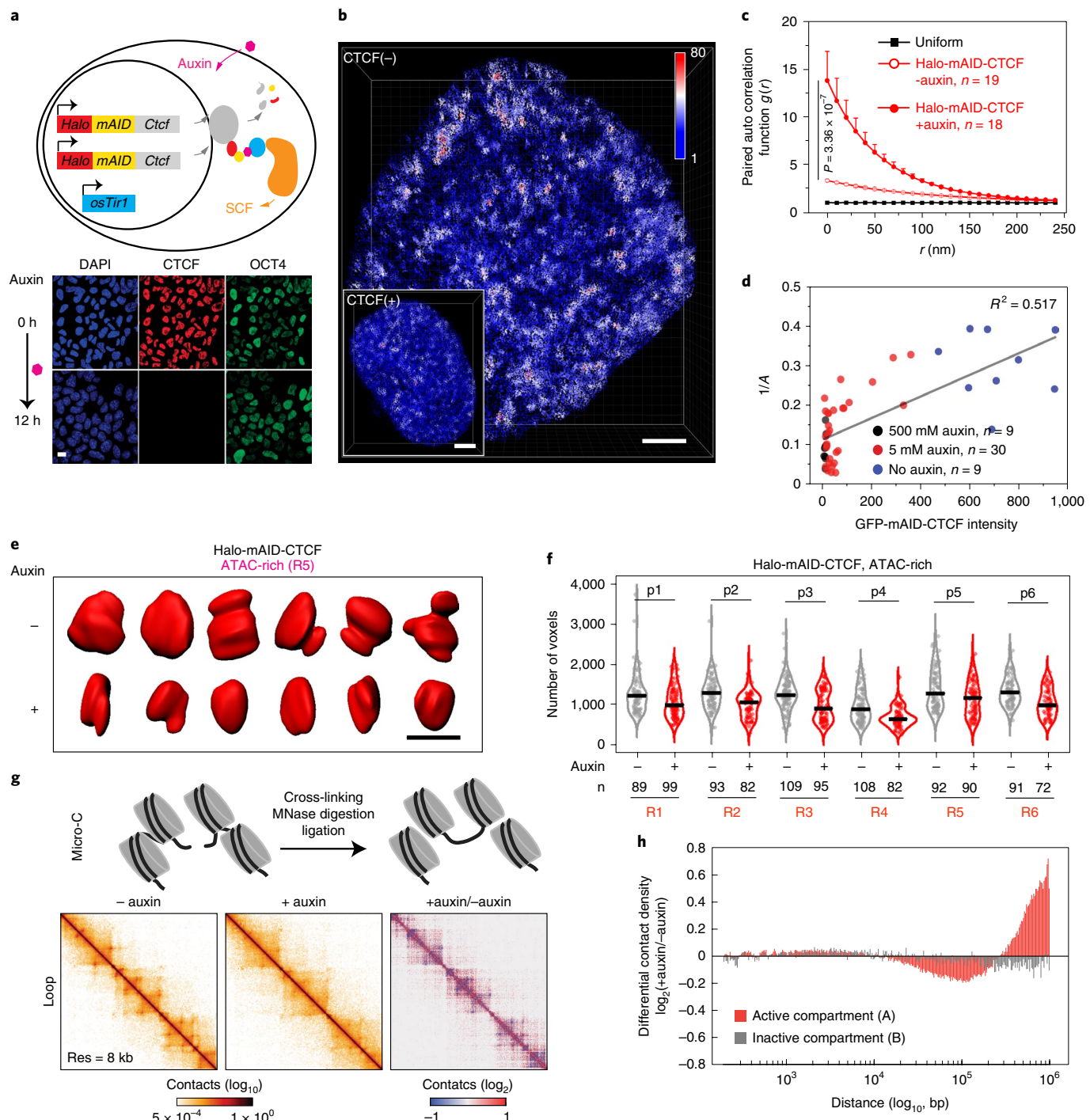
Discussion

Here we demonstrated that 3D ATAC-PALM enables super-resolution *in situ* imaging of the spatial organization of the accessible genome in different cell types of interest. 3D ATAC-PALM imaging in formaldehyde-fixed cells makes it potentially applicable to formalin fixed tissue slices and other clinical samples. The compatibility of 3D ATAC-PALM with Oligopaint DNA–FISH, RNA–FISH

and protein fluorescent imaging makes this method readily adaptable to researchers from a wide range of biomedical fields. We have demonstrated that 3D ATAC-PALM exhibits exquisite sensitivity to detect the spatial organizational changes of genome topology under a variety of chemical-genetic perturbations (TSA, CTCF depletion and so on), which are further validated by orthogonal approaches (Oligopaint DNA-FISH or Micro-C). We envision that this new single-cell super-resolution imaging method will complement existing genome imaging (DNA-FISH, CRISPR imaging and so on) and sequencing (Hi-C and so on) methods to understand fundamental principles underlying the 3D genome organization *in situ*.

The clustering of accessible chromatin unveiled by 3D ATAC-PALM highlights the prevalent spatial proximity among *cis*-regulatory elements, reminiscent of the extensive promoter–promoter,

enhancer–enhancer and enhancer–promoter interactions captured by ensemble chromatin interaction experiments^{39,40}. The architecture of clustered *cis*-regulatory elements may thus serve as a topological basis for mediating long-range enhancer–promoter communications and precise spatiotemporal gene expression control. In the future, high-throughput, sequence-specific Oligopaint DNA-FISH-based barcoding strategies^{27,41,42} in combination with 3D ATAC-PALM may help delineate the spatial relationship between ACDs, compartments, TADs and loops and the architectural basis of gene regulation. Integrating 3D ATAC-PALM with other functional (epi)genomic, genome editing and live-cell imaging approaches will facilitate dissecting fundamental mechanism and function of the spatial organization of the accessible genome. ATAC-seq has been applied to profile the human cancer landscape



and enables classification of cancer subtypes with important prognostic value⁴³. It will be of practical interest to use the exquisite spatial resolution of 3D ATAC-PALM to examine the accessible genomic landscape in disease specimens for clinical diagnosis and mechanistic investigations.

Online content

Any methods, additional references, Nature Research reporting summaries, source data, extended data, supplementary information, acknowledgements, peer review information; details of author contributions and competing interests; and statements of data and code availability are available at <https://doi.org/10.1038/s41592-020-0775-2>.

Received: 9 December 2019; Accepted: 11 February 2020;

Published online: 16 March 2020

References

- Dekker, J. et al. The 4D nucleome project. *Nature* **549**, 219–226 (2017).
- Dekker, J. et al. Capturing chromosome conformation. *Science* **295**, 1306–1311 (2002).
- Wit, E. De & Laat, W. De A decade of 3C technologies: insights into nuclear organization. *Genes Dev.* **26**, 11–24 (2012).
- Dekker, J. & Mirny, L. The 3D genome as moderator of chromosomal communication. *Cell* **164**, 1110–1121 (2016).
- Dekker, J., Marti-Renom, M. A. & Mirny, L. A. Exploring the three-dimensional organization of genomes: interpreting chromatin interaction data. *Nat. Rev. Genet.* **14**, 390–403 (2013).
- Finn, E. H. et al. Extensive heterogeneity and intrinsic variation in spatial genome organization. *Cell* **176**, 1502–1515 (2019).
- Levine, M., Cattoglio, C. & Tjian, R. Looping back to leap forward: transcription enters a new era. *Cell* **157**, 13–25 (2014).
- Wu, C. The 5' ends of *Drosophila* heat shock genes in chromatin are hypersensitive to DNase I. *Nature* **286**, 854–860 (1980).
- Boyle, A. P. et al. High-resolution mapping and characterization of open chromatin across the genome. *Cell* **132**, 311–322 (2008).
- Buenrostro, J. D., Giresi, P. G., Zaba, L. C., Chang, H. Y. & Greenleaf, W. J. Transposition of native chromatin for fast and sensitive epigenomic profiling of open chromatin, DNA-binding proteins and nucleosome position. *Nat. Methods* **10**, 1213–1218 (2013).
- Buenrostro, J. D. et al. Single-cell chromatin accessibility reveals principles of regulatory variation. *Nature* **523**, 486–490 (2015).
- Chen, X. et al. ATAC-seq reveals the accessible genome by transposase-mediated imaging and sequencing. *Nat. Methods* **13**, 1013–1020 (2016).
- Grimm, J. B. et al. Bright photoactivatable fluorophores for single-molecule imaging. *Nat. Methods* **13**, 985–988 (2016).
- Betzig, E. et al. Imaging intracellular fluorescent proteins at nanometer resolution. *Science* **313**, 1642–1645 (2006).
- Chen, B. C. et al. Lattice light-sheet microscopy: imaging molecules to embryos at high spatiotemporal resolution. *Science* **346**, 1257998 (2014).
- Legant, W. R. et al. High-density three-dimensional localization microscopy across large volumes. *Nat. Methods* **13**, 359–365 (2016).
- Huang, B., Wang, W., Bates, M. & Zhuang, X. Three-dimensional super-resolution imaging by stochastic optical reconstruction microscopy. *Science* **319**, 810–813 (2008).
- Peebles, P. J. E. Statistical analysis of catalogs of extragalactic objects. I. theory. *Astrophys. J.* **185**, 413 (1973).
- Sengupta, P. et al. Probing protein heterogeneity in the plasma membrane using PALM and pair correlation analysis. *Nat. Methods* **8**, 969–975 (2011).
- Ester, M., Kriegel, H. P., Sander, J. & Xu, X. A density-based algorithm for discovering clusters in large spatial databases with noise. In *Proc. 2nd International Conference on Knowledge Discovery and Data Mining (KDD '96)* 226–231 (AAAI Press, 1996).
- Sakae-Sawano, A. et al. Genetically encoded tools for optical dissection of the mammalian cell cycle. *Mol. Cell* **68**, 626–640 (2017).
- Kieffer-Kwon, K. R. et al. Myc regulates chromatin decompaction and nuclear architecture during B cell activation. *Mol. Cell* **67**, 566–578.e10 (2017).
- Beliveau, B. J. et al. Versatile design and synthesis platform for visualizing genomes with oligopaint FISH probes. *Proc. Natl Acad. Sci. USA* **109**, 21301–21306 (2012).
- Beliveau, B. J. et al. Single-molecule super-resolution imaging of chromosomes and *in situ* haplotype visualization using Oligopaint FISH probes. *Nat. Commun.* **6**, e7147 (2015).
- Boettiger, A. N. et al. Super-resolution imaging reveals distinct chromatin folding for different epigenetic states. *Nature* **529**, 418–422 (2016).
- Wang, S. et al. Spatial organization of chromatin domains and compartments in single chromosomes. *Science* **353**, 598–602 (2016).
- Bintu, B. et al. Super-resolution chromatin tracing reveals domains and cooperative interactions in single cells. *Science* **362**, eaau1783 (2018).
- Sabari, B. R. et al. Coactivator condensation at super-enhancers links phase separation and gene control. *Science* **361**, 387–392 (2018).
- Jin, C. H3.3/H2A.Z double variant-containing nucleosomes mark ‘nucleosome-free regions’ of active promoters and other regulatory regions. *Nat. Genet.* **41**, 941–945 (2009).
- Nora, E. P. et al. Targeted degradation of CTCF decouples local insulation of chromosome domains from genomic compartmentalization. *Cell* **169**, 930–944 (2017).
- Nishimura, K., Fukagawa, T., Takisawa, H., Kakimoto, T. & Kanemaki, M. An auxin-based degron system for the rapid depletion of proteins in nonplant cells. *Nat. Methods* **6**, 917–922 (2009).
- Wutz, G. et al. Topologically associating domains and chromatin loops depend on cohesin and are regulated by CTCF, WAPL, and PDS5 proteins. *EMBO J.* **36**, 3573–3599 (2017).
- Hsieh, T. H. S. Mapping nucleosome resolution chromosome folding in yeast by Micro-C. *Cell* **162**, 108–119 (2015).
- Hsieh, T.-H. S. et al. Resolving the 3D landscape of transcription-linked mammalian chromatin folding. Preprint at *bioRxiv* <https://doi.org/10.1101/638775> (2019).
- Fudenberg, G. et al. Formation of chromosomal domains by loop extrusion. *Cell Rep.* **15**, 2038–2049 (2016).
- Sanborn, A. L. et al. Chromatin extrusion explains key features of loop and domain formation in wild-type and engineered genomes. *Proc. Natl Acad. Sci. USA* **112**, E6456–E6465 (2015).
- Alipour, E. & Marko, J. F. Self-organization of domain structures by DNA-loop-extruding enzymes. *Nucleic Acids Res.* **40**, 11202–11212 (2012).
- Fudenberg, G., Abdennur, N., Imakaev, M., Goloborodko, A. & Mirny, L. A. Emerging evidence of chromosome folding by loop extrusion. *Cold Spring Harb. Symp. Quant. Biol.* **82**, 45–55.
- Li, G. et al. Extensive promoter-centered chromatin interactions provide a topological basis for transcription regulation. *Cell* **148**, 84–98 (2012).
- Xie, L. et al. A dynamic interplay of enhancer elements regulates Klf4 expression in naïve pluripotency. *Genes Dev.* **31**, 1795–1808 (2017).
- Chen, K. H., Boettiger, A. N., Moffitt, J. R., Wang, S. & Zhuang, X. Spatially resolved, highly multiplexed RNA profiling in single cells. *Science* **348**, 356–372 (2015).
- Shah, S. et al. Dynamics and spatial genomics of the nascent transcriptome by intron seqFISH. *Cell* **174**, 363–376.e16 (2018).
- Corces, M. R. et al. The chromatin accessibility landscape of primary human cancers. *Science* **362**, e1898 (2018).

Publisher's note Springer Nature remains neutral with regard to jurisdictional claims in published maps and institutional affiliations.

© The Author(s), under exclusive licence to Springer Nature America, Inc. 2020

Methods

Tn5 expression and purification. The plasmid pTXB1-Tn5 (Addgene no. 60240) was used to express the hyperactive Tn5 transposase fused with the MexE Intein and Chitin-binding domain¹⁴. Briefly, the pTXB1-Tn5 was transformed into the T7 Express lysY/Iq Competent *E. coli* (NEB, catalog no. C3013I). A 11 culture of transformed cells were grown in TB buffer with antibiotics at 37°C to an absorbance (A_{600}) of ~0.6 and induced with 0.25 mM IPTG. The cells were incubated at 23 °C for 4 h, collected and washed with 50 ml 1× PBS with cComplete Protease Inhibitor Cocktail (Roche). The cell pellet was snap frozen in liquid nitrogen, stored at -80°C overnight, resuspended in 160 ml HEGX (20 mM HEPES-KOH at pH 7.2, 0.8 M NaCl, 1 mM EDTA, 10% glycerol, 0.2% Triton X-100) with Protease Inhibitor and sonicated for ten cycles of 30 s ON/60 s OFF at 30 W output on a Model 100 Sonic Dismembrator (Fisher Scientific). The lysate was centrifuged in a Beckman JA25.50 rotor at 16,000 r.p.m. for 30 min at 4°C and 8.4 ml 5% neutralized PEI (Sigma P3143) was added dropwise into the supernatant with gentle agitation for 15 min at 4°C followed by another centrifuge at 13,000 r.p.m. for 10 min at 4°C. In the meantime, 20 ml Chitin Resin (NEB catalog no. S6651L) was equilibrated in a column with 200 ml of HEGX buffer supplemented with protease inhibitor and loaded with the supernatant from the PEI-centrifuge step by slow gravity flow (<0.3 ml min⁻¹). The column was washed with 400 ml HEGX overnight at a flow rate ~0.6 ml min⁻¹. To cleave the Tn5 from the Intein, 48 ml HEGX buffer + 100 mM DTT supplemented with protease inhibitor was loaded to the top of the column bed and the column was left closed for 48 h at 4°C. Cleaved Tn5 was eluted in ~1 ml fractions and Tn5 elution efficiency was monitored by the Pierce Coomassie (Bradford) Protein Assay Kit (Thermo Fisher Scientific catalog no. 23200). Fractions with the strongest absorbance were pooled and dialyzed versus two changes of 21 of 2× Tn5 dialysis buffer (100 mM HEPES-KOH at pH 7.2, 0.2 M NaCl, 0.2 mM EDTA, 2 mM DTT, 0.2% Triton X-100, 20% glycerol) at 4°C. After dialysis, the protein concentration was measured using a Nanodrop spectrophotometer (Thermo Scientific) and confirmed by running an SDS-PAGE gel using BSA as a standard. Tn5 protein was further concentrated to 20 mg ml⁻¹ using the Amicon Ultra-15 Centrifugal Filter Unit and we added 50% glycerol to the final concentrate and prepared aliquots in screw-top microcentrifuge tubes, flash freeze them in liquid nitrogen and stored them at -80°C. The Tn5 activity was tested by the in vitro tagmentation assay¹⁴ and further verified by performing genome-wide ATAC-seq experiment.

PA-JF₅₄₉ dye-oligo conjugation and purification. The mosaic ends (ME) adaptors for Tn5 transposase were synthesized by Integrated DNA Technologies with attachment of a 5' end primary amino group by a six-carbon spacer arm (C6). The oligonucleotide sequences and their modifications are:

Tn5ME-A: 5'-amino-C6-TCGTCCGCAGCGTCAGATGTTGATAAGAGACAG3'
 Tn5ME-B: 5'-amino-C6-GTCTCGTGGCTCGGAGATGTGATAAGAGA
 CAG-3'
 Tn5MEREV: 5'-(phos)CTGTCTCTTATACACATCT-3'

The PA-JF₅₄₉ coupled to the N-hydroxysuccinimide (NHS) ester (NHS-PA-JF₅₄₉) was synthesized by L. Lavis's group at the Janelia Research Campus. The NHS-PA-JF₅₄₉ was dissolved in anhydrous dimethylsulfoxide (DMSO) immediately before conjugation. The Tn5ME-A and Tn5ME-B oligos were first dissolved in deionized water and then extracted three times with chloroform. The upper aqueous solution was carefully extracted and precipitated by 3 M sodium acetate (pH 5.2) and ethanol. The pellet was washed with 70% ethanol, dried and dissolved in ultrapure water. The purified oligos were reacted with excessive NHS-PA-JF₅₄₉ in anhydrous DMSO (mass ratio 1:2.5) in the labeling buffer (0.1 M sodium tetraborate, pH 8.5). The reaction was incubated at room temperature for overnight (>12 h) with constant stirring and protection from light. The conjugation reaction was further precipitated by 3 M sodium acetate, pH 5.2 and ethanol. The purified pellet was dissolved in 0.1 M TEAA (triethylammonium acetate; Thermo Fisher Scientific catalog no. 400613).

Purification of oligo-dye conjugates were performed on Agilent 1200 Analytical high-performance liquid chromatography (HPLC) system equipped with an autosampler, diode array detector and fraction collector. The column used was Eclipse XDB-C18 column (4.6 × 150 mm² 5 μm, Agilent) and eluted with a linear gradient of 0–100% MeCN/H₂O with constant 10 mM TEAA additive; 30 min run; 1 ml min⁻¹ flow, detection at 260 nm. Sample fractions were pooled and lyophilized to obtain the product as white solid.

In vitro Tn5 transposome assembly, validation and preparation for PALM imaging. The HPLC purified Tn5ME-A-PA-JF₅₄₉, Tn5ME-B-PA-JF₅₄₉, Tn5MEREV oligos were resuspended in water to 100 μM each. Tn5ME-A-PA-JF₅₄₉ or Tn5ME-B-PA-JF₅₄₉ were mixed with Tn5MEREV in each molar ratio in 1× annealing buffer (10 mM Tris HCl pH 8.0, 50 mM NaCl, 1 mM EDTA) and were denatured on a benchtop thermocycler at 95°C for 5 min and then slowly cooled down to 25°C at the rate of -1 °C min⁻¹. We assembled the Tn5 transposome with PA-JF₅₄₉ according to previously published protocol¹² by combining 0.25 vol Tn5MEREV/Tn5ME-A-PA-JF₅₄₉ + Tn5MEREV/Tn5ME-B-PA-JF₅₄₉ (50 μM each), 0.4 vol glycerol (100% solution), 0.12 vol 2× dialysis buffer (100 mM HEPES-KOH at pH 7.2, 0.2 M NaCl, 0.2 mM EDTA, 2 mM DTT, 0.2% Triton X-100, 20% glycerol), 0.1 vol Tn5

(50 μM) and 0.13 vol H₂O, followed by gentle nutation at room temperature for 1 h. The activity of in-house prepared Tn5 transposome was validated by genome-wide ATAC-seq as described previously¹² following a reverse crosslinking step.

We prepared cells for 3D ATAC-PALM experiments as reported previously¹². Briefly, cells (mouse ESC or MEF) were plated onto no. 1 thickness 5 mm coverslips (Warner Instruments, catalog no. 64-0700) at around 70–80% confluence with proper coating 1 d before experiment. Cells were fixed with 1% paraformaldehyde (Electron Microscopy Sciences, catalog no. 15710) for 10 min at room temperature. After fixation, cells were washed three times with 1× PBS for 5 min and then permeabilized with ATAC lysis buffer (10 mM Tris-Cl, pH 7.4, 10 mM NaCl, 3 mM MgCl₂, 0.1% Igepal CA-630) for 10 min at room temperature. After permeabilization, the slides were washed twice in 1× PBS and put inside a humidity chamber box at 37°C. The transposase mixture solution (1× Tagmentation buffer: 10 mM Tris-HCl, pH 7.6, 5 mM MgCl₂, 10% dimethylformamide, 100 nM Tn5 PA-JF₅₄₉) was added to the cells and incubated for 30 min at 37°C inside the humidity chamber. After the transposase reaction, slides were washed three times with 1× PBS containing 0.01% SDS and 50 mM EDTA for 15 min at 55°C before mounted onto the lattice light-sheet microscope slot for 3D ATAC-PALM imaging.

3D ATAC-PALM image acquisition and processing. The 3D ATAC-PALM data were acquired by the lattice light-sheet microscopy¹⁵ at room temperature. The light sheet was generated from the interference of highly parallel beams in a square lattice and dithered to create a uniform excitation sheet. The inner and outer numerical apertures (NAs) of the excitation sheet were set to be 0.44 and 0.55, respectively. A Variable-Flow Peristaltic Pump (Thermo Fisher Scientific) was used to connect a 21 reservoir with the imaging chamber with 1× PBS circulating through at a constant flow rate. Labeled cells seeded on 5 mm coverslips (Warner Instruments) were placed into the imaging chamber and each image volume includes roughly 100–200 image frames, depending on the depth of field of view. Specifically, spontaneously activated PA-JF₅₄₉ dye were initially pushed into the fluorescent dark state through repeated photobleaching by scanning the whole image view with a 2 W 560 nm laser (MPB Communications Inc.). Then, the samples were imaged by iteratively photoactivating each plane with very low intensity 405 nm light (<0.05 mW power at the rear aperture of the excitation objective and 6 W cm⁻² power at the sample) for 8 ms and by exciting each plane with a 2 W 560 nm laser at its full power (26 mW power at the rear aperture of the excitation objective and 3.466 W cm⁻² power at the sample) for 20 ms exposure time. The specimen was illuminated when laser light went through a custom 0.65 NA excitation objective (Special Optics) and the fluorescence generated within the specimen was collected by a detection objective (CFI Apo LWD 25× W, 1.1 NA, Nikon), filtered through a 440/521/607/700 nm BrightLine quad-band bandpass filter (Semrock) and N-BK7 Mounted Plano-Convex Round cylindrical lens ($f=1000$ mm, $\varnothing 1"$, Thorlabs) and eventually recorded by an ORCA-Flash 4.0 sCMOS camera (Hamamatsu). The cells were imaged under sample scanning mode and the dithered light sheet at 500 nm step size, thereby capturing a volume of ~25 × 51 × (~27–54) μm³, considering the 32.8° angle between the excitation direction and the stage moving plane. All measurements were taken from distinct cells.

To precisely analyze the 3D ATAC-PALM data, we embedded nano-gold fiducials within the coverslips for drift correction as previously described¹⁶. 3D ATAC-PALM Images were taken to construct a 3D volume when the sample was moving along the *s* axis. Individual volumes per acquisition were automatically stored as Tiff stacks, which were then analyzed by in-house scripts written in MATLAB. The cylindrical lens introduced astigmatism in the detection path and recorded each isolated single molecule with its ellipticity, thereby encoding the 3D position of each molecule relative to the microscope focal plane. All processing was performed by converting all dimensions to units of *xy* pixels, which were 100 × 100 nm² after transformation due to the magnification of the detection objective and tube lens. We estimated the localization precision by calculating the standard deviation of all the localizations coordinates (*x*, *y* and *z*) after the nano-gold fiducial correction. The localization precision is 26 ± 3 nm and 53 ± 5 nm for *x*, *y* and *z*, respectively.

Raw 3D ATAC-PALM images were processed following previous published procedures^{15,16}. Specifically, a background image with gray values taken without illumination was subtracted from each frame of the current raw image. Photoactivated images were then filtered by subtracting Gaussian filtered images at two different standards:

$$I_{\text{filtered}} = I_{\text{raw}} \otimes K_{\text{low}} - I_{\text{raw}} \otimes K_{\text{high}} \quad (1)$$

where *I* represents the photon number of raw images after converting counts to photons using the manufacturer-provided calibration curve, \otimes is the convolution operator, and K_{low} and K_{high} represent 5 × 5 pixel two-dimensional Gaussian function with standard deviation $\sigma=2$ (low) and 1 (high):

$$K = 2\pi^{-3/2}\sigma^{-2} e^{-\frac{(x-3)^2}{2\sigma^2}-\frac{(y-3)^2}{2\sigma^2}} \quad (2)$$

The local maxima were then determined on these filtered images and the coordinates were estimated and used as the true position of the isolated single molecule.

To precisely determine the z position of each isolated localization, cylindrical lenses were used and the corresponding astigmatic PSF function could be formulated as a Gaussian function with separate x and y deviations. These deviations encoded the relative z -offset of the signal with respect to the focal plane.

$$\text{PSF}(x, y, z) = \frac{1}{2\pi\sigma_x\sigma_y} e^{-\left(\frac{x^2}{2\sigma_x^2} + \frac{y^2}{2\sigma_y^2}\right)} \quad (3)$$

where

$$\sigma_x = c_1 + c_2 z + c_3 z^2$$

$$\sigma_y = c_4 + c_5 z + c_6 z^2$$

Here, σ_x and σ_y were polynomial function of z . The constants c_1-c_6 can be fitted by scanning bright and regular beads through the focal plane using piezoelectric stage.

To rigorously compare ATAC localizations within the nucleus, an image stack for H2B-GFP stably expressed in mouse ESCs was captured before the 3D ATAC-PALM experiment under the same lattice light-sheet microscopy imaging condition. The image stack of the GFP channel was deskewed and deconvoluted using the same algorithm to identify a nuclear mask to segment 3D ATAC-PALM signal. The percentage of localizations falling into the same volume in or out of the mask were counted and plotted in Supplementary Fig. 2b. We found that most (>95%) localizations fall into the nuclear H2B mask, suggesting that the manual segmentation based on 3D ATAC-PALM signal intensity is sufficient to distinguish it from out-of-nucleus signal (for example, mitochondria) or nonspecific background.

To derive the 3D ATAC-PALM intensity map to compare with HP1-GFP labeled heterochromatin spatial distribution, ATAC localizations were binned within a cubic of 100 nm with a 3D Gaussian filter and a convolution kernel of $3 \times 3 \times 3$.

3D pair autocorrelation function, pair cross-correlation function and Ripley's function. As described previously⁴⁵, the pair correlation function $g_0(r)$ or radial distribution function measures the probability P of finding a localization of accessible chromatin in a volume element dV at a separation r from another accessible chromatin site:

$$P = \rho g_0(r) dV \quad (5)$$

where ρ represents the mean density of accessible chromatin in the nucleus.

3D $g_0(r)$ was computed by

$$g_0(r) = \frac{3V}{4\pi(3r^2\Delta r + 3r\Delta r^2 + \Delta r^3)} \frac{1}{N(N-1)} \sum_{i=1}^N \sum_{j \neq i}^N \delta(r - r_{ij}) \quad (6)$$

where N is the total number of localizations and V is the 3D nuclear volume, and $\Delta r = 50$ nm is the binning width used in the analysis. The item $4\pi(3r^2\Delta r + 3r\Delta r^2 + \Delta r^3)/3$ represents the shell-shape volume between the search radius from r to $r + \Delta r$. The Dirac delta function is defined by

$$\delta(r - r_{ij}) = \begin{cases} 1, & r - r_{ij} \leq \Delta r \\ 0, & r - r_{ij} > \Delta r \end{cases} \quad (7)$$

where r_{ij} represents the pair-wise Euclidean distance between localization point i and j . To eliminate the boundary effect in calculation of $g_0(r)$ from a finite 3D volume, we generated $g_r(r)$ from uniform distributions with the same localization density in the same volume as real data using the MATLAB convex hull function. Accordingly, the final normalized 3D pair autocorrelation function $G(r)$ was calculated by:

$$G(r) = \frac{g_0(r)}{g_r(r)} \quad (8)$$

Similarly, the 3D pair cross-correlation function $c_0(r)$ between localizations of molecule A and those of molecule B can be formulated as

$$c_0(r) = \frac{3V}{4\pi(3r^2\Delta r + 3r\Delta r^2 + \Delta r^3)} \frac{1}{MN} \sum_{i=1}^M \sum_{j=1}^N \delta(r - r_{ij}) \quad (9)$$

where M is the total number of localizations for molecule A and N is the total number of localizations for molecule B. The Dirac delta function is defined as the same as in equation (7). Similarly, the final normalized 3D pair autocorrelation function $C(r)$ was calculated by:

$$C(r) = \frac{c_0(r)}{c_r(r)} \quad (10)$$

where $c_r(r)$ refers to the pair cross-correlation function calculated from uniform distributions with the same localization density in the same volume as real data used.

Ripley's K function is a variation of pair correlation function to study point distribution patterns and is defined by the equation:

$$K(r) = \frac{V}{N-1} \left[\frac{1}{N} \sum_{i=1}^N \sum_{i \neq j} \delta_K(r - r_{ij}) \right] \quad (11)$$

where its delta function given by

$$\delta_K(r - r_{ij}) = \begin{cases} 1, & r - r_{ij} \leq 0 \\ 0, & r - r_{ij} > 0 \end{cases}$$

The $K(r)$ for a random Poisson distribution is πr^2 . Therefore, its derivative Ripley's L function is given by

$$L(r) = \sqrt{\frac{K(r)}{\pi}} \quad (12)$$

The deviation of $L(r)$ from expected random Poisson distribution can be used to indicate point clustering or dispersion. The further normalized Ripley's H function

$$H(r) = L(r) - r \quad (13)$$

which can be used to estimate the point clustering and domain size⁴⁶.

Whereas $G(r)$ can be used as bona fide criteria for estimating the clustering effect of a group of spatial localizations, it has to be adjusted regarding the inevitable localization uncertainty of the PSF. If the distribution is purely random, the revised pair autocorrelation $G_R(r)$ considering PSF uncertainty is given by

$$G_R(r) = G_{\text{PSF}}(r) + 1 \quad (14)$$

with

$$G_{\text{PSF}}(r) = \frac{1}{8\pi^{3/2}\sigma^3} e^{-r^2/4\sigma^2} \quad (15)$$

where ρ represents the average surface density of molecules, $G_{\text{PSF}}(r)$ denotes the correlation of uncertainty in the PSF and σ for standard deviation. The spatial autocorrelation of accessible chromatin can be approximated by an exponential function:

$$g(r) = Ae^{-r/\epsilon} + 1 \quad (16)$$

where ϵ and A denote the correlation length and amplitude of the accessible chromatin cluster, respectively. The total correlation can be described by

$$G(r) = G_{\text{PSF}}(r) + (Ae^{-r/\epsilon} + 1) \otimes G_{\text{PSF}}(r) \quad (17)$$

The raw data were fitted by using equation (17) to derive $g(r)$ and parameters A and ϵ . The approximated function $g(r)$ was used throughout the paper for pair autocorrelation analysis. Curve fitting was performed using the trust-region method implemented in the Curve Fitting MATLAB toolbox.

Since over-counting does not give rise to apparent coclustering in double label experiments when pair cross-correlation functions are measured⁴⁷, $C(r)$ can serve as bona fide criteria for estimating the coclustering effect of spatial localizations from two different channels without additional adjustment.

Two-dimensional pair cross-correlation function and autocorrelation function.

To calculate the spatial cross-correlation between the two-color ATAC localization signal and the heterochromatin HP1 α signal, we first converted the localization densities into intensity map via two-dimensional Gaussian blurring. The pair cross-correlation function $c(\vec{r})$ was then calculated by the fast Fourier transform (FFT) method described previously⁴⁵.

$$c(\vec{r}) = \Re \left\{ \frac{\text{FFT}^{-1}(\text{FFT}(I_1) \times \text{conj}[\text{FFT}(I_2)])}{\rho_1 \rho_2 N(\vec{r})} \right\} \quad (18)$$

$$N(\vec{r}) = \text{FFT}^{-1}(|\text{FFT}(\text{Mask})|^2) \quad (19)$$

The $N(\vec{r})$ is the autocorrelation of a mask matrix that has the value of 1 inside the nucleus used for normalization. $\text{conj}[]$ refers to complex conjugate, ρ_1 and ρ_2 are the average surface densities (number of localizations divided by the surface area) of images I_1 and I_2 and $\Re\{\cdot\}$ indicates the real part. The FFT and its inverse (FFT and FFT^{-1}) were computed by `fft2()` and `ifft2()` functions in MATLAB, respectively. Cross-correlation functions were calculated first by converting the Cartesian coordinates to polar coordinates by MATLAB's `cart2pol()` function, binning by radius and by averaging within the assigned bins.

DBSCAN analysis. The density-based clustering algorithm DBSCAN was adopted to map and visualize individual local ACDs (core DBSCAN MATLAB code from <http://yarpiz.com/255/ypml110-dbscan-clustering>). The algorithm first finds neighboring data points inside a sphere of radius r , and adds them into same group. In parallel, a predefined threshold minimal points ($minPts$) was used by the algorithm to justify whether any counted group is a cluster. If the number of points in a group is less than the threshold $minPts$, the data point is classified as noise. As a negative control, we generated uniformly sampled data sets with the same localization density as our ATAC localizations. We then implemented DBSCAN analysis by using 150 nm as the searching radius (r) (peak radius from the Ripley's H function analysis) and empirically setting $minPts$ at ten. To reconstruct the *iso*-surface for each identified ACD, the convex hull that contains the ACD data points was calculated and visualized by using MATLAB. The volume of the convex hull was computed, and the normalized cluster radius (calculated from a sphere with equal volume) was estimated and shown in a violin plot.

Additional methods involved in this study are included in the Supplementary Note.

Statistical analysis. Statistical analysis was carried out using Origin and GraphPad Prism. Unless stated specifically, data are presented as mean \pm s.e.m. (standard error) with statistical significance (* $P < 0.05$, ** $P < 0.01$, *** $P < 0.001$, with the exact P values in the figure legends). All values of n are provided in the figure legends. We used nonparametric two-tailed Mann–Whitney U -tests unless indicated in the figure legends.

Reporting Summary. Further information on research design is available in the Nature Research Reporting Summary linked to this article.

Data availability

The raw and processed next-generation sequencing data was deposited to NCBI GEO with public accession number [GSE126112](#). The source data for figures and extended figures are available online as Source Data. Other data supporting the findings of this study are available from the corresponding authors upon reasonable request.

Code availability

The software for identifying, localizing and plotting single-molecule data is freely available after execution of a research license with HHMI. The codes for the $g(r)$ and DBSCAN analysis is freely available from https://github.com/ammondongp/3D_ATAC_PALM.

References

44. Picelli, S. et al. Tn5 transposase and tagmentation procedures for massively scaled sequencing projects. *Genome Res.* **24**, 2033–2040 (2014).
45. Liu, Z. et al. 3D imaging of Sox2 enhancer clusters in embryonic stem cells. *eLife* **3**, 1–29 (2014).
46. Kiskowski, M. A., Hancock, J. F. & Kenworthy, A. K. On the use of Ripley's K -function and its derivatives to analyze domain size. *Biophys. J.* **97**, 1095–1103 (2009).
47. Veatch, S. L. et al. Correlation functions quantify super-resolution images and estimate apparent clustering due to over-counting. *PLoS ONE* **7**, e31457 (2012).

Acknowledgements

We thank X. Darzacq, S. Chong, T. Graham, D. McSwiggen and C. Cattoglio for critical reading of the manuscript, the Tjian-Darzacq laboratory members for helpful discussions and P. Sengupta and H. Rouault for advice on data analysis. We thank D. Walpita and K. Schaefer with assistance for fluorescence-activated cell sorting experiments, D. Alcor for Airyscan Imaging and M. Radcliff for assistance. This work is supported by the Howard Hughes Medical Institute (HHMI) and the Janelia Visitor Program. Y.F.Q. and B.Z. acknowledge support by the National Science Foundation Grant MCB-1715859. H.Y.C. acknowledges support by NIH grant P50-HG007735. X.C. is supported by Swedish Research Council International Postdoctoral Fellowship (VR-2016- 06794) and starting grant (VR-2017-02074), Jeansson foundation grant (JS2018-0004) and a Vleugl grant. W.R.L. acknowledges support from the Searle Scholars Program, the Beckman Young Investigator Program, an NIH New Innovator Award (DP2GM136653) and the Packard Fellows Program.

Author contributions

L.X. and Z.L. conceived and designed the study. L.X., P.D., T.-H.S.H. and X.C. performed the experiments and analyzed the data. L.X., P.D., Z.L. and R.T. wrote the manuscript. Z.L. and R.T. supervised the study.

Competing interests

The authors declare no competing interests.

Additional information

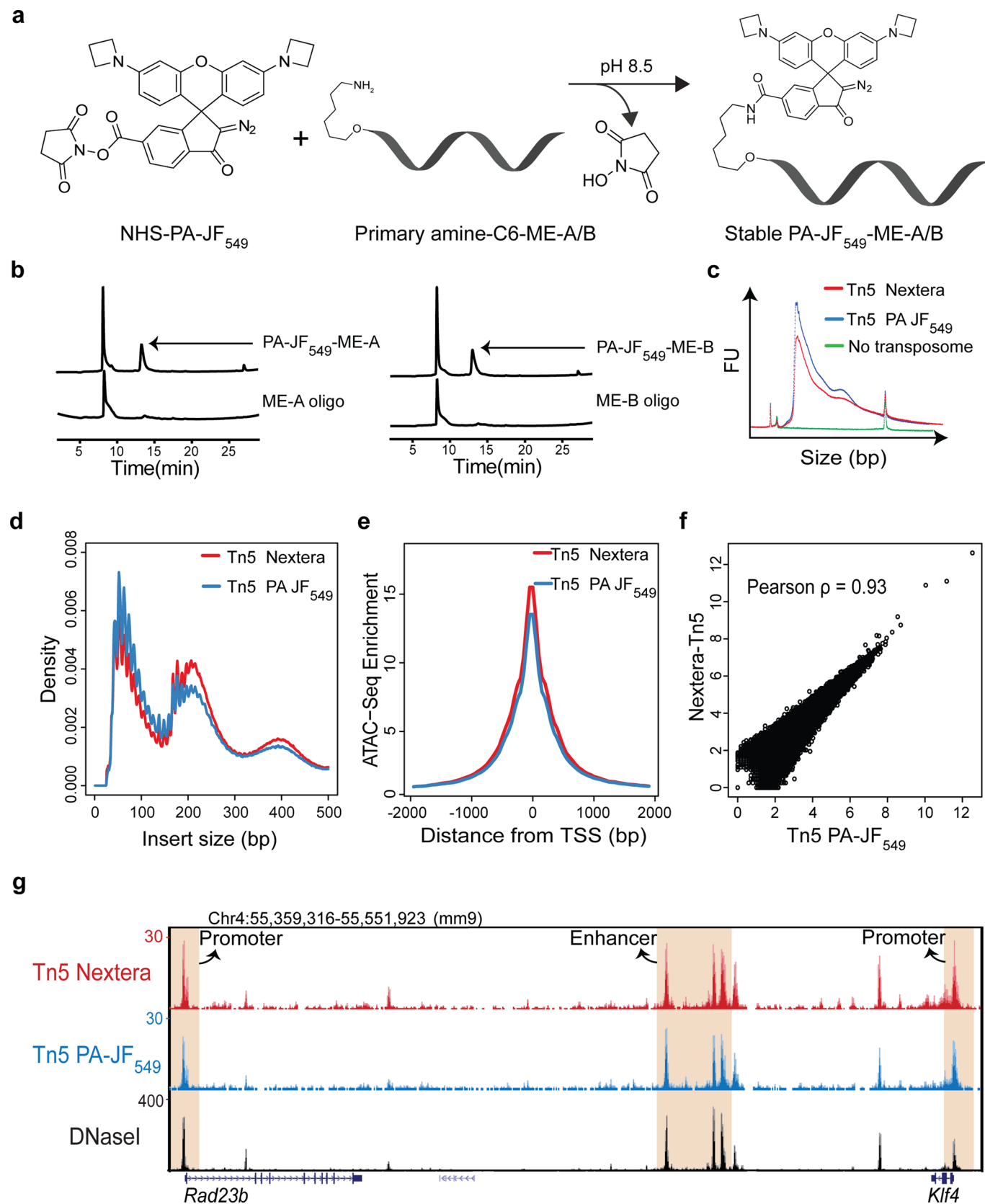
Extended data is available for this paper at <https://doi.org/10.1038/s41592-020-0775-2>.

Supplementary information is available for this paper at <https://doi.org/10.1038/s41592-020-0775-2>.

Correspondence and requests for materials should be addressed to R.T. or Z.L.

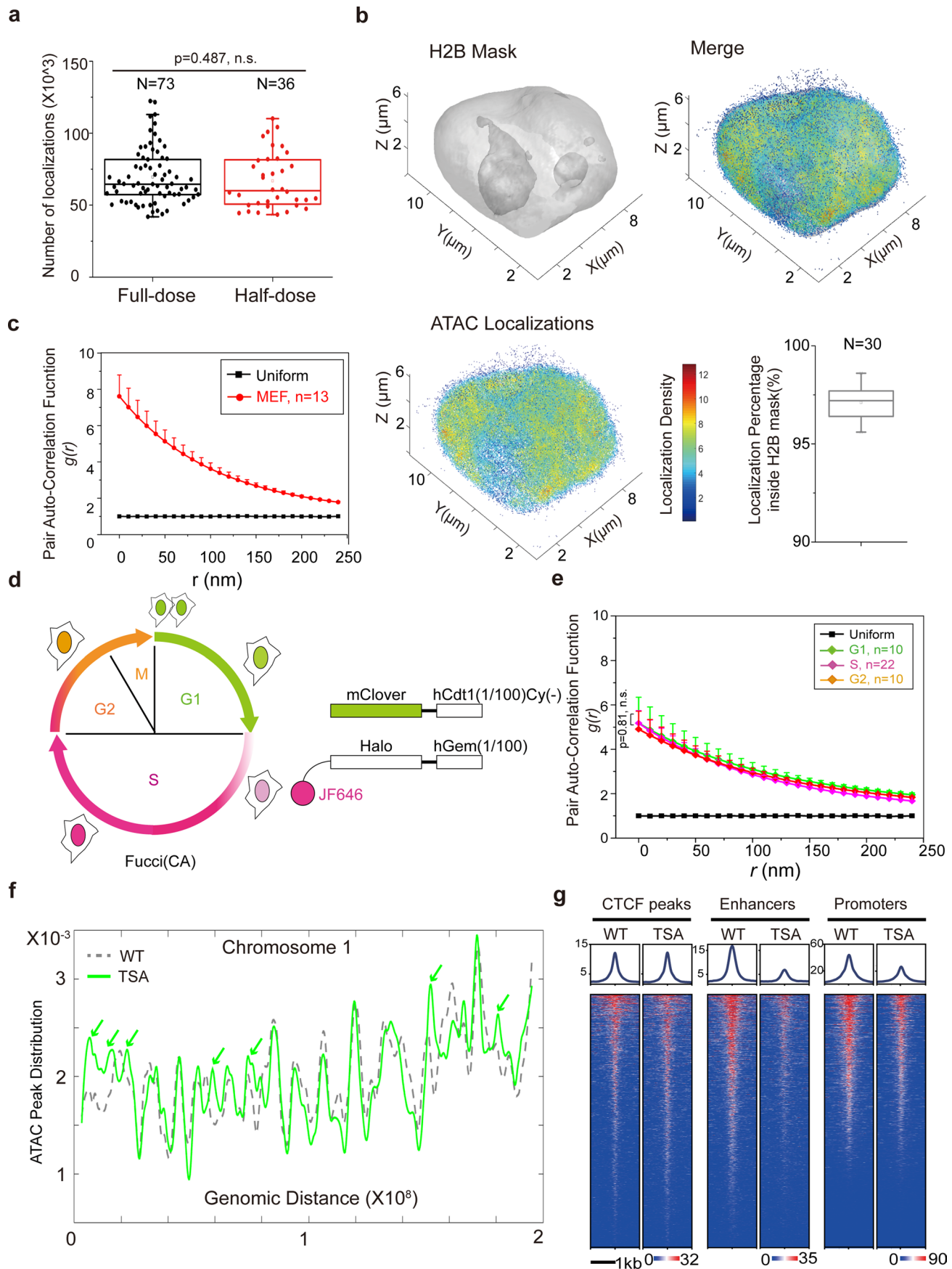
Peer review information Rita Strack was the primary editor on this article and managed its editorial process and peer review in collaboration with the rest of the editorial team.

Reprints and permissions information is available at www.nature.com/reprints.



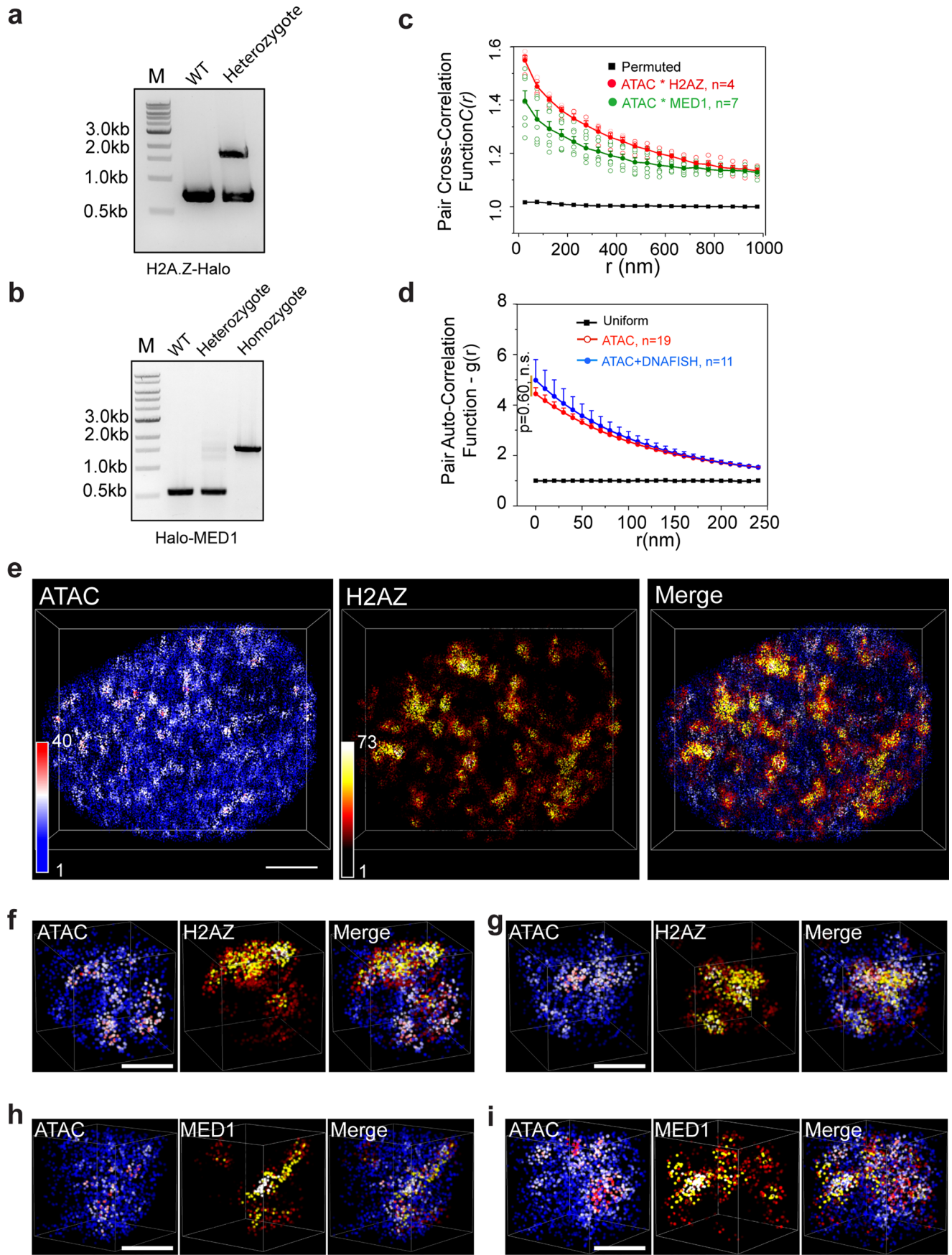
Extended Data Fig. 1 | See next page for caption.

Extended Data Fig. 1 | 3D ATAC-PALM labeling strategy. **a**, N-hydroxysuccinimide (NHS) ester chemical conjugation chemistry. PA-JF₅₄₉ dye coupled with the NHS ester reacts with the primary amine group on the Tn5 ME oligos to yield the stable dye-oligo conjugate via the covalent amide bond. **b**, The chromatogram of PA-JF₅₄₉ NHS ester and oligo amine reaction by reverse phase High Pressure Liquid Chromatography (HPLC). The oligo-dye stable conjugates (smaller peaks as indicated by arrows) were selectively purified. Representative image from n = 3 independent experiments. **c**, Fragmentation analysis of *in vitro* constituted Tn5-PA-JF₅₄₉ and Nextera Tn5 transposome by combining the Tn5 transposome with mouse genomic DNA followed by PCR and an electropherogram analysis by Bioanalyzer. A reaction without transposase was used as a negative control. **d-f**, Genome-wide comparison of ATAC-seq libraries prepared from mouse ESCs by using either in-house prepared Tn5 PA-JF₅₄₉ or commercially available Nextera Tn5. The ATAC-seq experiment for Tn5 PA-JF₅₄₉ was performed after 3D ATAC-PALM imaging from the same sample. The comparison was made by analyzing the insert size distribution (**d**), the enrichment around transcription start sites (TSS) (**e**) and at all ATAC-seq peaks (**f**). In (**f**), a Pearson correlation coefficient was calculated by genome-wide correlation analysis. **g**, Representative tracks for Tn5 PA-JF₅₄₉ ATAC-seq, Nextera Tn5 ATAC-seq and DNasel-seq (ENCODE) data illustrated by using UCSC genome browser. *Cis*-regulatory elements representing promoters (for *Klf4* and *Rad23b* genes) and enhancers (for *Klf4* gene) are highlighted in the shaded area. Experiments in Fig. c-g were repeated twice with similar results.



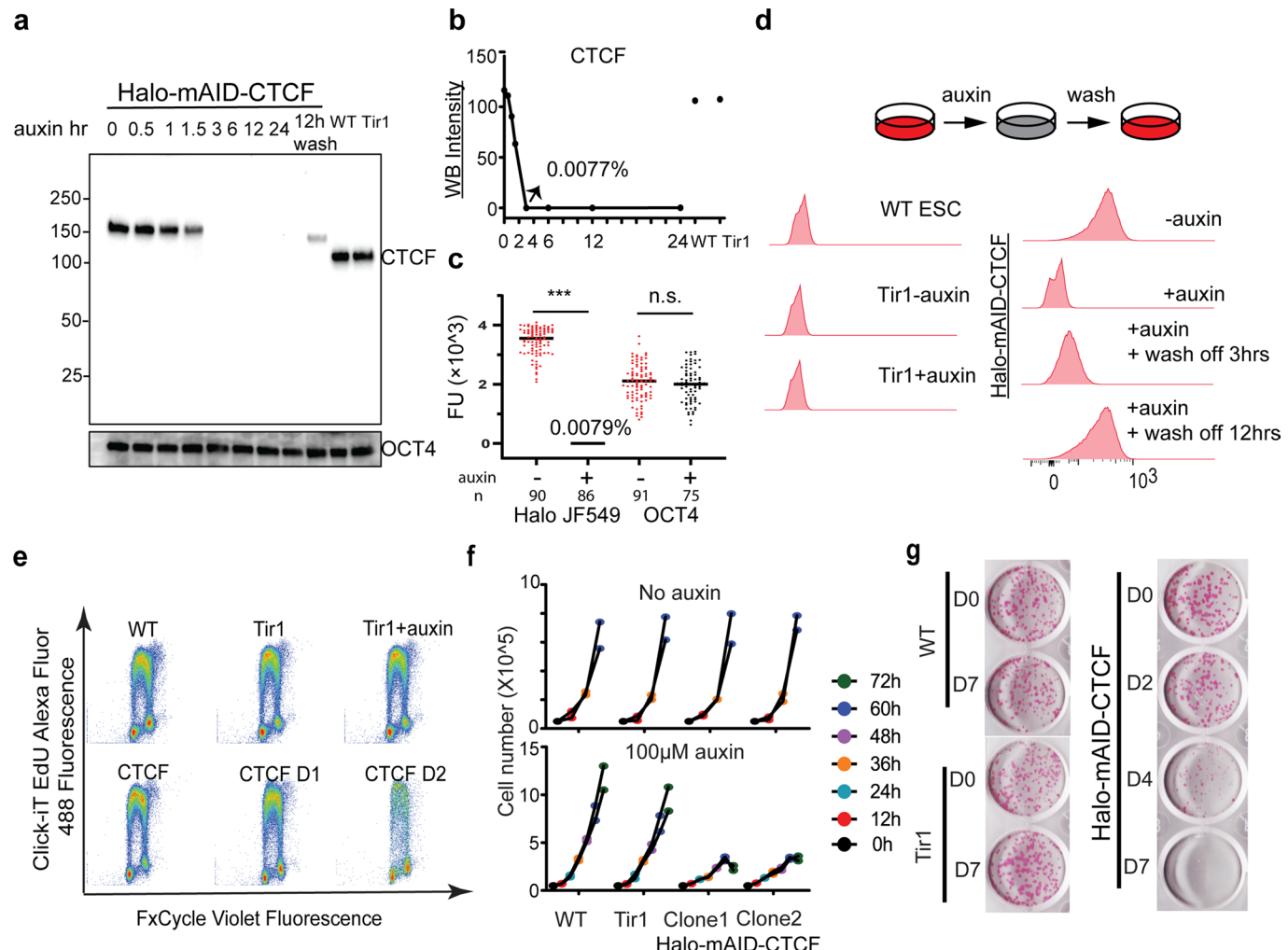
Extended Data Fig. 2 | See next page for caption.

Extended Data Fig. 2 | Characterization of 3D ATAC-PALM localizations. **a**, The box plot compares the number of 3D ATAC-PALM localizations in the full-dose (73 cells, ~100 nM Tn5 PA-JF₅₄₉) and half-dose (36 cells, ~50 nM) labeling conditions. The middle line represents median. The two-sided Student's t-test was performed. **b**, ATAC-PALM localizations (lower left) were separated as in-nucleus and out-nucleus fractions based on the H2B-GFP mask (upper left). The merged image was shown in the upper right panel. The color bar indicates the localization density calculated by using a canopy radius of 250 nm. Lower right panel shows the percentage of localizations falling into the H2B-GFP mask from 30 cells. The middle line represents median. **c**, Pair auto-correlation function $g(r)$ of ATAC-PALM localizations calculated for MEFs. The center curve represents the mean value and the error bars represent S.E.M. **d**, Schematics for the FUCCI(ICA) system in which the first 100 amino acids of hCdt1 lacking the Cy motif (1/100) Cy(-) is fused to mClover and the first 100 amino acids of hGeminin is fused to HaloTag stained by the JF₆₄₆ HaloTag ligand. G1 phase cells exhibit only green and S phase cells display only far red fluorescence, whereas dual color positive cells correspond to G2/M phase. **e**, Pair auto-correlation function $g(r)$ for ATAC-PALM localizations calculated across different cell cycle phases. The error bars represent S.E.M. The two-sided Mann-Whitney U test was performed. **f**, ATAC-seq peak density distribution in the WT (grey line) and TSA treated (green line) cells for each of 500 bins across chromosome 1. Green arrowheads indicate new accessible chromatin induced by TSA treatment. **g**, Heatmaps of ATAC-seq signal were plotted over CTCF binding sites (putative insulator sites), enhancers (defined by H3K27ac ChIP-seq) and promoter regions in the mouse genome with DMSO or TSA treatment (50 μM, 6h). Statistics source data are provided in Source Data Extended Fig. 2.



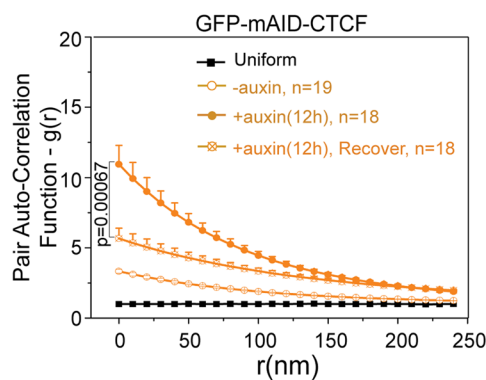
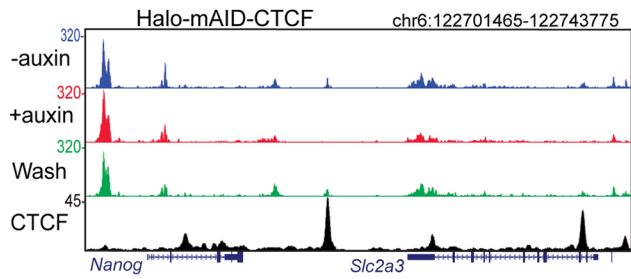
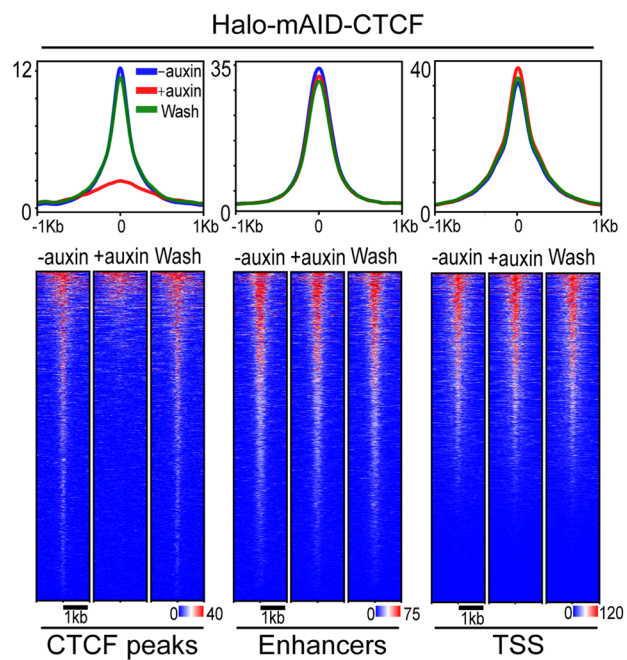
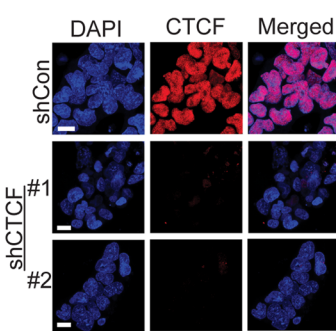
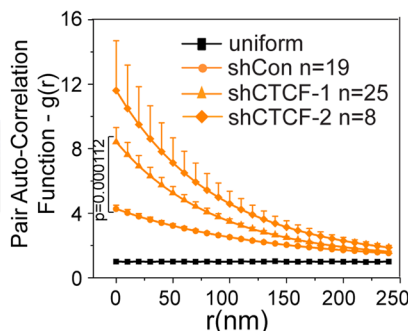
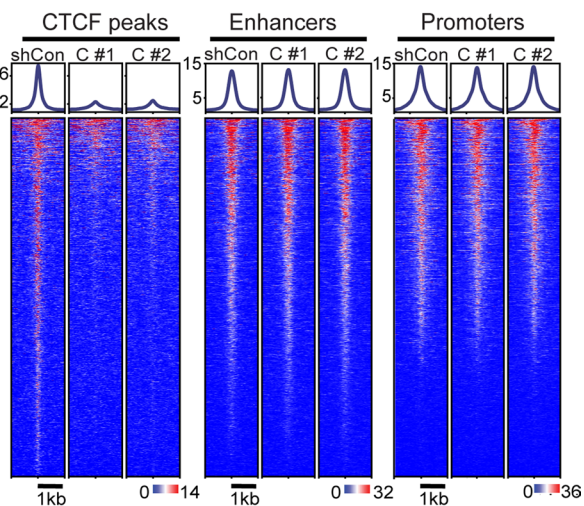
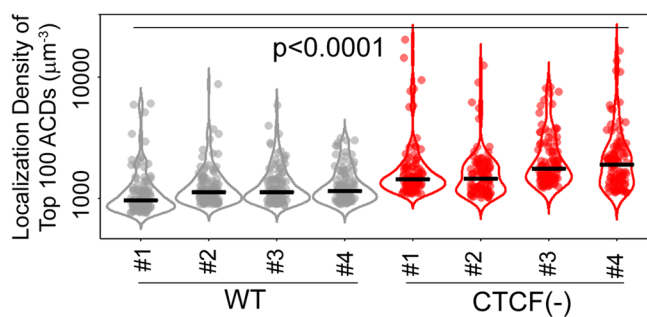
Extended Data Fig. 3 | See next page for caption.

Extended Data Fig. 3 | Two-color 3D PALM imaging of accessible chromatin and landmark proteins in the active chromatin. **a** and **b**, PCR genotyping validates the correct knock-in of HaloTag in frame with histone variant H2A.Z (**a**) or Mediator subunit MED1 (**b**) coding sequence in mESCs. We obtained heterozygous and homozygous HaloTag labeling to endogenous H2A.Z and MED1, respectively. All knock-in cells were validated by Sanger sequencing. Experiments were repeated two times. **c**, 2D pair cross-correlation function $C(r)$ calculated for accessible chromatin localizations and H2A.Z or MED1, in contrast to that of HP1 in Fig. 2g. Circles represent mean values for cross-correlation function at a given radius (r). The error bars represent S.E.M. **d**, Comparison of pair auto-correlation function $g(r)$ calculated with ATAC labeling alone and ATAC labeling - DNA FISH condition. The error bars represent S.E.M. The two-sided Mann-Whitney U test was performed. Experiments were repeated three times. **e**, 3D illustration of colocalized accessible chromatin and HaloTag labeled H2A.Z protein localizations within a single nucleus. The color-coded localization density was calculated with a canopy radius of 250 nm. Scale bar: 2 μ m. The accessible chromatin was labelled with PA-JF₅₄₉, while H2A.Z-HaloTag molecules were labelled with PA-JF₆₄₆. **f** and **g**, 3D illustration of colocalized accessible chromatin and HaloTag labeled H2A.Z protein localizations in representative sub-regions with volume of 2 μ m \times 2 μ m \times 2 μ m. Scale bar: 1 μ m. **h** and **i**, 3D illustration of colocalized accessible chromatin and HaloTag-MED1 protein localizations in representative sub-regions with volume of 2 μ m \times 2 μ m \times 2 μ m. Scale bar: 1 μ m. Experiments were repeated 3 times and data were pooled together for analysis for (**d**)–(**h**). Statistics source data are provided in Source Data Extended Fig. 3.



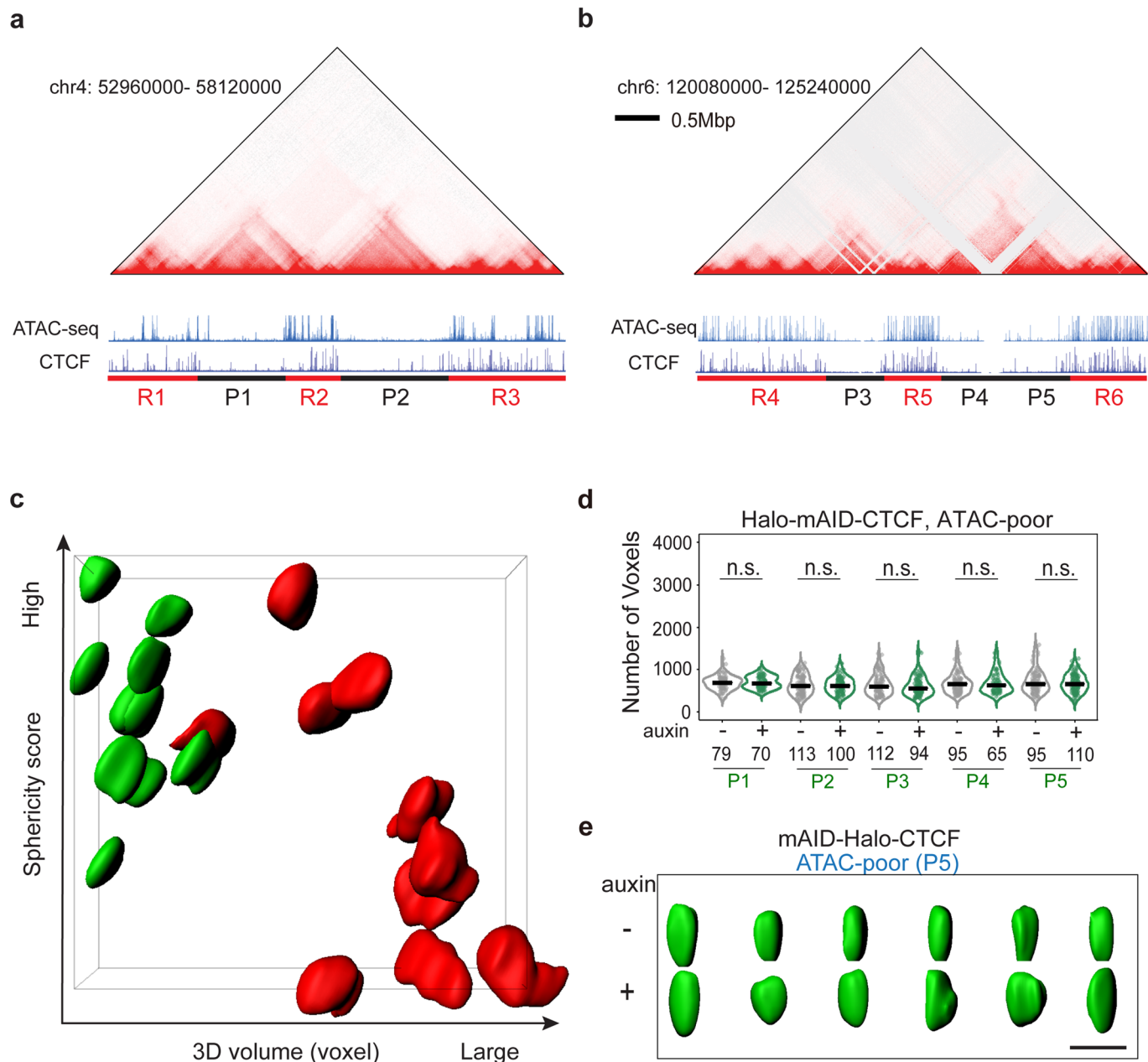
Extended Data Fig. 4 | Efficient depletion of CTCF by the AID degron system. **a**, Western blotting (WB) analysis of endogenous HaloTag-mAID-CTCF at indicated time points after the auxin treatment and wash off recovery with OCT4 as the internal control. **b**, Quantifying WB intensity as grey scale values for the corresponding WB bands in **(a)**. **c**, Single cell analysis of HaloTag-mAID-CTCF and OCT4 protein levels after auxin treatment. HaloTag-mAID-CTCF was stained with 100nM HaloTag ligand JF₅₄₉ and OCT4 was detected by immunofluorescence. FU stands for arbitrary fluorescent unit, with extra-cellular background subtracted. The middle line represents mean fluorescence value. Experiment was repeated two times for **(a)-(c)** with similar results.

Two-sided Mann-Whitney U test was used for analysis with p value for Halo JF549 group < 0.0001 and for OCT4 group 0.3232. **d**, Flow cytometry analysis of CTCF levels before (-auxin), after (+auxin) auxin treatment and after auxin wash off. The parent Tir1 ES cells (Tir1 - Auxin; Tir1 + Auxin) were used as the negative control. ~50,000 gated live cells were recorded and analyzed for each condition. Experiments were repeated three times. **e**, DNA synthesis analysis of HaloTag-mAID-CTCF ESCs by the Click-iT EdU labeling kit at the indicated time points (D, Days) after auxin treatment. Experiments were performed two times and representative images are shown. **f**, Cell proliferation analysis of Wild type (WT), parental Tir1, and two clones of Halo-mAID-CTCF ESCs. Upper panel, without auxin treatment, different cell lines showed similar growth rates. Lower panel, acute CTCF depletion significantly slowed down cell proliferation after 36 hours (two-tailed Student's t-test with p value < 0.05). Data from two technical replicates from two N-CTCF-mAID clones were shown. **g**, Single cell colony formation assay by alkaline phosphatase staining for WT, parental Tir1, and Halo-mAID-CTCF ESCs at indicated time points after auxin treatment. Biological replicates n = 2. Statistics source data are provided in Source Data Extended Fig. 4.

a**c****b****d****e****f****g**

Extended Data Fig. 5 | See next page for caption.

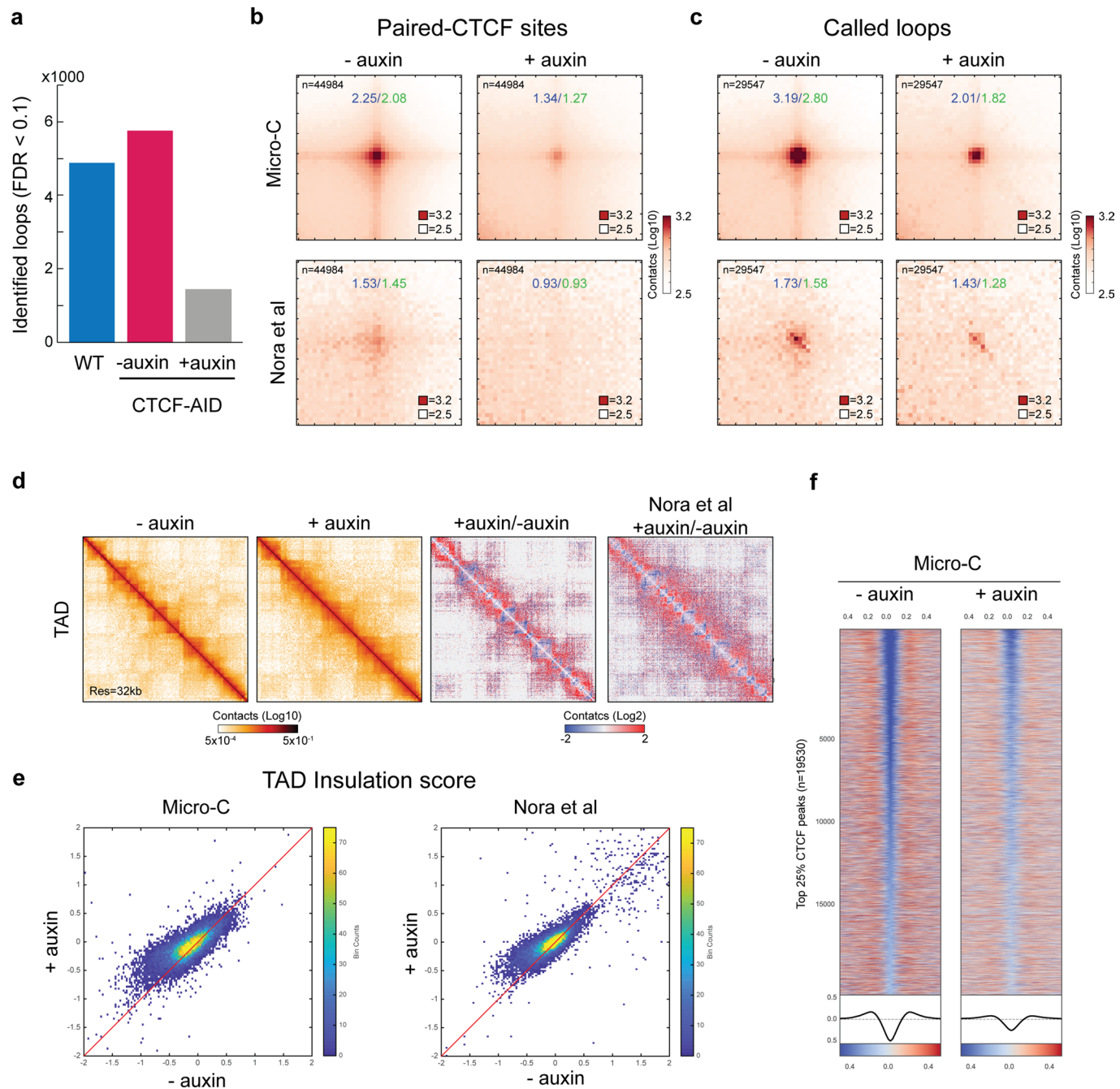
Extended Data Fig. 5 | Enhanced clustering of ACDs upon CTCF depletion. **a**, Pair auto-correlation function $g(r)$ of ATAC-PALM localizations from GFP-mAID-CTCF ESCs under normal, auxin-treated and auxin wash-off (~24 hours) conditions. The error bars represent S.E.M. Two-sided Mann-Whitney U test was performed. **b**, HaloTag-mAID-CTCF cells were processed for genome-wide ATAC-seq analysis under conditions including without auxin, auxin treatment and washout after auxin treatment. Three biological replicates were performed. **c**, ATAC-seq enrichment at a representative genomic region under normal (-auxin), auxin-treated (+auxin) and recovery conditions for HaloTag-mAID-CTCF cells. CTCF ChIP-seq track is displayed below as a reference. Experiments were performed 3 times. **d**, Bi-allelic CTCF-HaloTag knock-in cells were infected with either lentiviral particles containing the empty vector (shCon) or lentiviral vectors expressing two independent shRNAs against CTCF (#1 and #2). Cells were selected with Puromycin for two days and stained with 200nM JF₅₄₉ HaloTag ligand and DAPI before confocal imaging. Biological replicates $n = 2$. **e**, Enhanced accessible chromatin clustering after shRNA mediated CTCF knockdown, which was monitored by staining cells with 200nM JF₆₄₆. The $g(r)$ analysis of 3D ATAC-PALM localizations showed significant increased $g(0)$ in CTCF knockdown cells, compared with control cells. The curve center represents the mean and the error bar represents S.E.M. The two-sided Mann-Whitney U test was performed. **f**, CTCF knockdown cells were processed for genome-wide ATAC-seq analysis. CTCF knockdown by both shRNAs (C #1 and C #2) markedly reduced the chromatin accessibility at CTCF binding sites compared to shCon cells without significantly affecting that at enhancers and promoters. **g**, Violin plot of localization density of top 100 rank ordered ACDs among 4 individual cells for each condition. The black bar indicates the median value. For statistical test, data from 4 individual cells for each condition were pooled together and two-sided Mann-Whitney U test was applied. Statistics source data are provided in Source Data Extended Fig. 5.



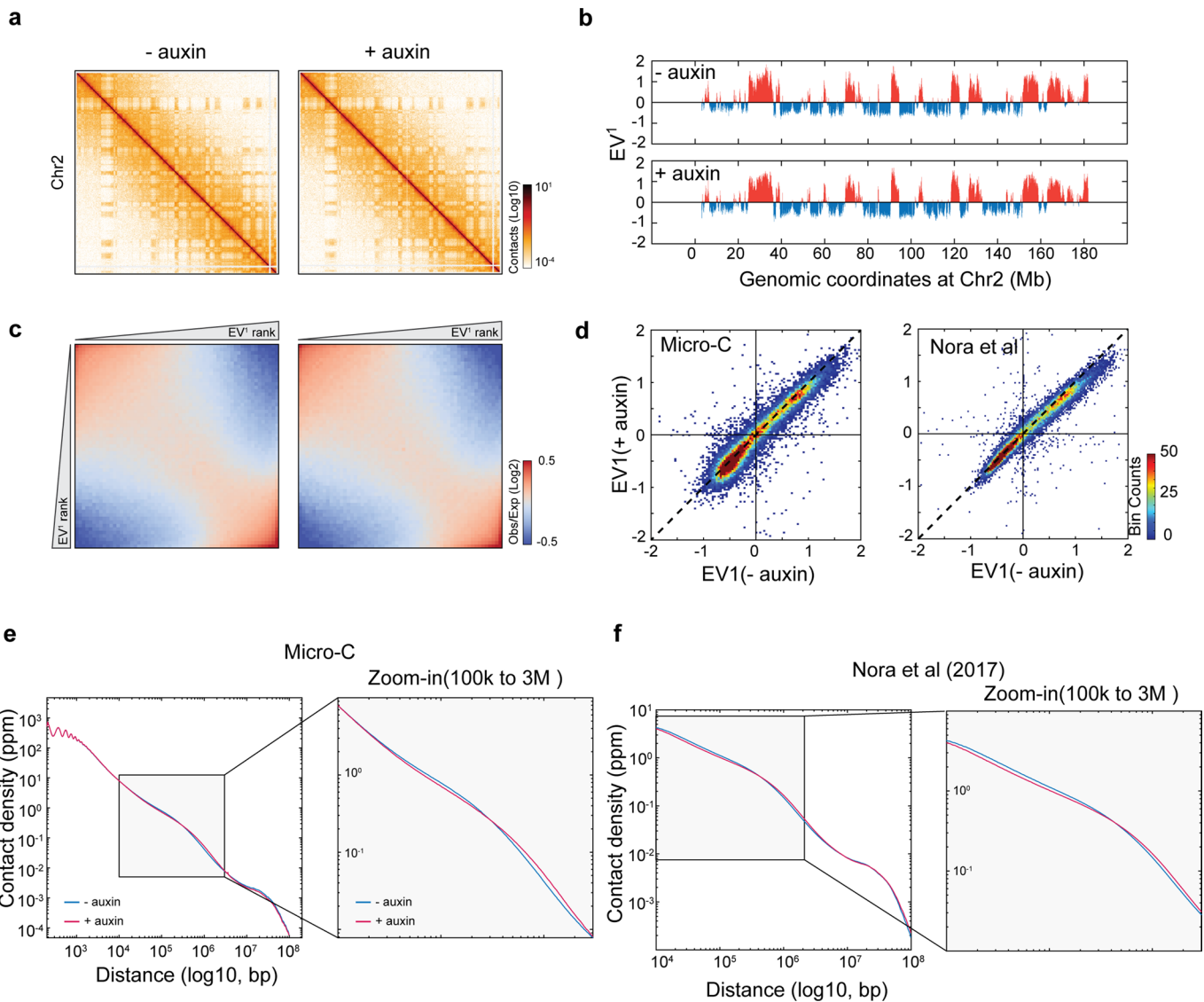
Extended Data Fig. 6 | Measuring structural changes of ATAC-rich and ATAC-poor segments upon CTCF depletion by Oligopaint DNA-FISH.

a-b, Alignment of Hi-C heatmap, ATAC-seq, CTCF ChIP-seq tracks for two chromosomal regions harboring pluripotency genes *Klf4* (Chr4) and *Nanog* (Chr6). ATAC-rich (R1-6; red) and ATAC-poor (P1-5; black) segments are underlined. The sizes of each domain are R1(633kb), P1(1133kb), R2(643kb), P2(1100kb), R3(1120kb), R4(1250kb), P3(740kb), R5(640kb), P4(690kb), P5(690kb), R6(990kb). See details on the domain coordinates in the Methods.

c, Two-dimensional sphericity score and 3D volume (by voxels) plot of all the ATAC-rich and ATAC-poor segments (*iso-surfaces*) in Supplementary Video 6 marked by 3D Oligopaint DNA-FISH probes. **d**, Violin plot of 3D volumes (the number of voxels) of five ATAC-poor segments (P1-P5) before and after CTCF depletion. Throughout the volume measurements in this study, each voxel size is $x=48.9\text{ nm}$, $y=48.9\text{ nm}$, $z=199\text{ nm}$. The number (n) of alleles analyzed is indicated at the bottom. The black bar indicates the median value for each data set and two-sided Mann-Whitney U test was applied for statistical test. P-values for P1-P5 are: p1=0.585, p2=0.932, p3=0.226, p4=0.849, p5=0.853. **e**, Representative *iso-surfaces* of an ATAC-poor segment (P5, green) before (-) and after (+) CTCF depletion (12 hours). Scale bar, 1 μm . Biological replicates $n=3$. Statistics source data are provided in Source Data Extended Fig. 6.



Extended Data Fig. 7 | CTCF depletion significantly reduced the number of loops and the degree of TAD domain insulation by high-resolution Micro-C analysis. **a**, Number of loops in WT-mESC, CTCF-AID mESC -auxin, and +auxin conditions. We identified a similar number of loops in WT-mESC ($n=4887$) and CTCF-AID mESC -auxin ($n=5764$), while only 1442 loops were identified after CTCF depletion under identical loop calling criteria. We performed two biological replicates and the data was pooled for analysis. **b-c**, Aggregate peak analysis on paired-CTCF sites or called loops from Micro-C and Hi-C¹ data. Loops were greatly disrupted in Micro-C data after CTCF depletion, which showed a 1.67-fold decrease at CTCF sites or 1.59-fold decrease at called loop loci, respectively. We obtain much fewer loops from previous Hi-C data likely due to the lower resolution¹. **d**, Snapshots of Micro-C contact maps on chr8:80M-95M at 32-kb resolution. Contact maps showed more inter-TAD contacts (loss of insulation) and modestly higher inter-compartment domain contacts after CTCF depletion. Hi-C data also showed a similar result but with a slightly different plaid-like pattern. **e**, Heatmap of insulation strength at CTCF-binding sites. Insulation strength was over 2-fold decrease at the top 25% of CTCF binding sites after CTCF depletion. **f**, Scatter plots of insulation strength at the called boundaries. Micro-C and Hi-C both showed consistent insulation loss (higher insulation score) after CTCF depletion.



Extended Data Fig. 8 | CTCF depletion significantly increased the contact probability in A compartment by high-resolution Micro-C analysis.

a, Snapshots of Micro-C contact maps on the entire Chr2, showing the plaid-like compartments before and after auxin-mediated CTCF depletion (6 hours). **b**, Compartment analysis by principle component analysis (PCA). The plots showed the eigenvector of the first PCA. Positive value is compartment A, and negative value is compartment B. There is no noticeable change in the large-scale compartment organization after CTCF depletion. **c**, Genome-wide analysis of the compartment strength. The saddle plot showed the contact probability between compartments and showed B-B on the top-left corner and A-A on the bottom-right corner. There is no significant compartment change after CTCF depletion. **d**, Comparison of compartment change in Micro-C and Hi-C. No dramatic change was found, albeit Micro-C appears to capture more changes in compartment strength than Hi-C after CTCF depletion. **e-f**, Genome-wide contact probability decaying curve by Micro-C (**e**) and Hi-C (**f**). See also Fig. 3h. Data from two biological replicates was pooled for analysis.

Reporting Summary

Nature Research wishes to improve the reproducibility of the work that we publish. This form provides structure for consistency and transparency in reporting. For further information on Nature Research policies, see [Authors & Referees](#) and the [Editorial Policy Checklist](#).

Statistics

For all statistical analyses, confirm that the following items are present in the figure legend, table legend, main text, or Methods section.

n/a Confirmed

- The exact sample size (n) for each experimental group/condition, given as a discrete number and unit of measurement
- A statement on whether measurements were taken from distinct samples or whether the same sample was measured repeatedly
- The statistical test(s) used AND whether they are one- or two-sided
Only common tests should be described solely by name; describe more complex techniques in the Methods section.
- A description of all covariates tested
- A description of any assumptions or corrections, such as tests of normality and adjustment for multiple comparisons
- A full description of the statistical parameters including central tendency (e.g. means) or other basic estimates (e.g. regression coefficient) AND variation (e.g. standard deviation) or associated estimates of uncertainty (e.g. confidence intervals)
- For null hypothesis testing, the test statistic (e.g. F , t , r) with confidence intervals, effect sizes, degrees of freedom and P value noted
Give P values as exact values whenever suitable.
- For Bayesian analysis, information on the choice of priors and Markov chain Monte Carlo settings
- For hierarchical and complex designs, identification of the appropriate level for tests and full reporting of outcomes
- Estimates of effect sizes (e.g. Cohen's d , Pearson's r), indicating how they were calculated

Our web collection on [statistics for biologists](#) contains articles on many of the points above.

Software and code

Policy information about [availability of computer code](#)

Data collection

Lattice Light Sheet Scope Imaging software (self-developed in HHMI/Janelia); LSM880 imaging software (Carl Zeiss); ZEN Black (Carl Zeiss); Bcl2tofastq2 v2.17 (Illumina)

Data analysis

Image J (downloaded in 2017 from NIH); Imaris 9.1 (Bitplane); Matlab 2015a (The Mathworks); Graphpad Prism 5 (Graphpad software); OriginPro 9.1 (OriginLab); Cutadapt; Bowtie2; Samtools; MACS2; FlowJo. All scripts, raw and processed images used in the paper were available from the corresponding author.

For manuscripts utilizing custom algorithms or software that are central to the research but not yet described in published literature, software must be made available to editors/reviewers. We strongly encourage code deposition in a community repository (e.g. GitHub). See the Nature Research [guidelines for submitting code & software](#) for further information.

Data

Policy information about [availability of data](#)

All manuscripts must include a [data availability statement](#). This statement should provide the following information, where applicable:

- Accession codes, unique identifiers, or web links for publicly available datasets
- A list of figures that have associated raw data
- A description of any restrictions on data availability

The raw sequencing data was deposited to NCBI GEO with accession number GSE126112. Other data, reagents and codes used to generate figures in this study are available upon reasonable request

Field-specific reporting

Please select the one below that is the best fit for your research. If you are not sure, read the appropriate sections before making your selection.

- Life sciences Behavioural & social sciences Ecological, evolutionary & environmental sciences

For a reference copy of the document with all sections, see nature.com/documents/nr-reporting-summary-flat.pdf

Life sciences study design

All studies must disclose on these points even when the disclosure is negative.

Sample size	The sample size was determined by data availability and no sample size pre-calculation was performed by statistical method. Due to the extensive heterogeneity of genome folding, we typically collected ~100 objects for Oligopaint and ~10-30 cells for 3D ATAC-PALM, to ensure sufficient representation of variability of the results.
Data exclusions	Single molecule tracking data with significant cellular movement during acquisition were removed from further analysis.
Replication	All experiments were replicated twice as indicated in the Methods section and were successful.
Randomization	Not relevant in this study. Samples were allocated as either wild type/control group or chemical/genetic treatment group.
Blinding	Investigators were not blinded to group allocation. However, all quantitative analysis were performed in the same way for both control and treatment group to avoid bias.

Reporting for specific materials, systems and methods

We require information from authors about some types of materials, experimental systems and methods used in many studies. Here, indicate whether each material, system or method listed is relevant to your study. If you are not sure if a list item applies to your research, read the appropriate section before selecting a response.

Materials & experimental systems		Methods	
n/a	Involved in the study	n/a Involved in the study	
<input type="checkbox"/>	Antibodies	<input type="checkbox"/>	ChIP-seq
<input type="checkbox"/>	Eukaryotic cell lines	<input type="checkbox"/>	Flow cytometry
<input checked="" type="checkbox"/>	Palaeontology	<input checked="" type="checkbox"/>	MRI-based neuroimaging
<input checked="" type="checkbox"/>	Animals and other organisms		
<input checked="" type="checkbox"/>	Human research participants		
<input checked="" type="checkbox"/>	Clinical data		

Antibodies

Antibodies used	CTCF (Millipore, catlog number 07729), OCT4 (Santa Cruz, catlog number sc-5279)
Validation	The OCT4 antibody has been used in 1443 publications (https://www.scbt.com/p/oct-3-4-antibody-c-10) to detect mouse OCT4 protein by IF, WB et al. The CTCF primary antibody specificity is further verified in our CTCF inducible depletion mouse ESC cell lines by WB (Extended Figure 4 a-b).

Eukaryotic cell lines

Policy information about cell lines	
Cell line source(s)	JM8.N4 mouse ESCs was derived from the C57BL/6N strain MEF: isolated from 14 d.p.c of pregnant mice (C57BL/6N strain). Lenti-X™ 293T Cell Line: purchased from Takara Bio, Catlog number 632180
Authentication	The JM8.N4 cells were authenticated by short tandem repeat DNA profiling and approved by the NIH 4D Nucleome project as a Tier2 cell line. MEFs were not authenticated.
Mycoplasma contamination	The JM8.N4 cells and 293T cells were tested for Mycoplasma contamination and were negative. MEFs cells were not tested.
Commonly misidentified lines (See ICLAC register)	No commonly misidentified cell lines were used in this study.

ChIP-seq

Data deposition

- Confirm that both raw and final processed data have been deposited in a public database such as [GEO](#).
- Confirm that you have deposited or provided access to graph files (e.g. BED files) for the called peaks.

Data access links

May remain private before publication.

The raw ATAC-seq and Micro-C files were deposited to NCBI GEO with accession number GSE126112. To review GEO accession GSE126112:
 Go to <https://www.ncbi.nlm.nih.gov/geo/query/acc.cgi?acc=GSE126112>
 We have made the data public.

Files in database submission

GSM3591784 Nextera_ATAC_seq
 GSM3591785 PA549_Tn5_ATAC_seq
 GSM3591786 WT_NoTSA_control_ATAC_seq
 GSM3591787 6h_TSA_ATAC_seq
 GSM3591788 AID_Halo_CTCF_noauxin_ATAC_seq
 GSM3591789 AID_Halo_CTCF_12hauxin_ATAC_seq
 GSM3591790 AID_Halo_CTCF_auxin_washoff_ATAC_seq
 GSM3591791 shCon_ATAC_seq
 GSM3591792 shCTCF-1_ATAC_seq
 GSM3591793 shCTCF-2_ATAC_seq
 GSM4047028 Micro-C_CTCF_noauxin_rep1
 GSM4047029 Micro-C_CTCF_auxin_6hour_rep1
 GSM4047030 Micro-C_CTCF_noauxin_rep2
 GSM4047031 Micro-C_CTCF_auxin_6hour_rep2

Genome browser session (e.g. [UCSC](#))

UCSC, m10

Methodology

Replicates

GSM3591784 Nextera_ATAC_seq has only one measurement. Other ATAC-seq experiments have been replicated at least twice and achieved reproducible results.

Sequencing depth

All ATAC-seq libraries were sequenced to appropriate depth(>20 million reads per sample). All ATAC-seq libraries were generated with pair-end sequencing at Illumina HiSeq 2500 or NextSeq 500/550 high and/or mid throughput 150 cycles.

Antibodies

No antibodies were used in ATAC-seq experiments.

Peak calling parameters

ATAC-seq peaks were called using the MACS2 callpeak function using the -f BAMPE parameter.

Data quality

We use fragment length distribution, TSS enrichment, reads within peaks as previously described (Chen X, Nature Methods, 2016) to validate the quality of ATAC-seq data.

Software

We use common open source software/codes to analyze the ATAC-seq data including : Bowtie2, Samtools, Cutadapt, MACS2, deeptools2.

Flow Cytometry

Plots

Confirm that:

- The axis labels state the marker and fluorochrome used (e.g. CD4-FITC).
- The axis scales are clearly visible. Include numbers along axes only for bottom left plot of group (a 'group' is an analysis of identical markers).
- All plots are contour plots with outliers or pseudocolor plots.
- A numerical value for number of cells or percentage (with statistics) is provided.

Methodology

Sample preparation

JM.8N4 ESCs were trypsinized,re-suspended in single cell suspension in PBS, and passed through a filter to remove doublets before sorting or analysis. To sort for HaloTag positive cells after genome engineering, we pre-stained the cells with JF549 HaloTag ligand for 30min and washed three times for 3X5min before FACS sorting.

Instrument

We used the CytoFLEX S system (Beckman) for cell proliferation analysis (Click-iT® EdU Alexa Fluor® 488 Flow Cytometry Assay Kit).

Software

We used the standard Beckman FACS software for recording and FlowJo to analyze FACS data.

Cell population abundance

typically 50,000 cells were recorded for cell cycle analysis.

Gating strategy

Gating strategy was determined by a negative control cell without any fluorescent staining.

Tick this box to confirm that a figure exemplifying the gating strategy is provided in the Supplementary Information.